Materials Advances

ROYAL SOCIETY OF CHEMISTRY

PAPER

View Article Online
View Journal | View Issue

Check for updates

Cite this: *Mater. Adv.*, 2026, 7, 1584

Synergistic effects of metal-modified carbon nanotubes: experimental characterization and theoretical modeling for energy and environmental solutions

Govindhasamy Murugadoss, *[a] Nachimuthu Venkatesh, [a] Narthana Kandhasamy,[a] Irina Zaporotskova, [b] Durai Govindarajan, [c] Natesan Kumaresan, [d] Kamalan Kirubaharan, [e] Uday Kumar Khanapuram *[f] and Soorathep Kheawhom *[c]

Received 28th August 2025,
Accepted 14th December 2025

DOI: 10.1039/d5ma00974j

rsc.li/materials-advances

Metal-functionalized carbon nanotubes (CNTs) have emerged as versatile nanostructures with tunable properties for energy conversion, storage, and environmental remediation. In this study, we integrate experimental investigations with theoretical modeling to explore the structure–property relationships and multifunctional performance of CNTs decorated with transition metal nanoparticles (Ni, Cu, Ag) and their synergistic combinations (Ni–Cu–Ag). A scalable and facile synthesis route was employed to fabricate these nanocomposites, which were thoroughly characterized to evaluate their structural, morphological, optical, and surface chemical features. The metal-functionalized CNTs demonstrated significant enhancements in oxygen evolution reaction (OER) activity, capacitive energy storage, and photocatalytic degradation of organic pollutants. Notably, the ternary CNT–Ni–Cu–Ag nanocomposite exhibited outstanding OER performance with an overpotential of 382 mV at 50 mA cm^{-2} and a Tafel slope of 73 mV dec^{-1}, along with a high specific capacitance of 1451 F g^{-1} and excellent stability (98% retention after 5000 cycles). Furthermore, the material achieved remarkable photocatalytic degradation efficiencies of ciprofloxacin (98.5%) and diclofenac sodium salt (86%) within 120 minutes under visible light. Complementary density functional theory (DFT) simulations revealed the preferential adsorption of metal nanoparticles on the CNT surface and their role in modulating the electronic band structure, thereby rationalizing the enhanced catalytic and optoelectronic behaviour. These results highlight the promise of metal-functionalized CNTs as multifunctional platforms for next-generation energy conversion, storage, and environmental remediation technologies.

1. Introduction

Global energy demand and fossil fuel depletion pose urgent environmental challenges, driving the need for clean, sustainable alternatives. Rising CO_2 emissions, climate change, and reliance on energy-intensive processes make renewable energy conversion and storage vital. MXenes, MOFs, and carbon-based nanomaterials are being explored to overcome efficiency and stability limits in solar, fuel, and storage devices.[1,2] Among them, carbon nanotubes (CNTs) stand out due to their exceptional mechanical strength, electrical conductivity, and thermal stability. CNTs can be synthesised *via* CVD, arc discharge, or laser ablation, with functionalization enhancing their electrochemical performance.[3] They are widely applied in supercapacitors, batteries, and other applications, offering high capacitance, rapid charge/discharge, and long cycle life and improve charge transport and light absorption.[4,5] One-dimensional CNTs have found extensive use as carbon supports for enhancing electrocatalytic reactions, leveraging their exceptional properties, such as high electronic conductivity, substantial edge/basal plane ratios, anti-fouling ability, and extensive surface area.[6–8] Consequently, when combined with

---

[a] *Centre for Nanoscience and Nanotechnology, Sathyabama Institute of Science and Technology (Deemed to be University), Chennai, Tamil Nadu 600 119, India. E-mail: murugadoss_g@yahoo.com*
[b] *Volgograd State University, 100 University Ave., Volgograd 400062, Russia*
[c] *Department of Chemical Engineering, Faculty of Engineering, Chulalongkorn University, Bangkok 10330, Thailand. E-mail: Soorathep.K@chula.ac.th*
[d] *Department of Physics, SSN Research Centre, Sri Sivasubramaniya Nadar College of Engineering, Chennai 603110, Tamil Nadu, India*
[e] *Coating Department, FunGlass – Centre for Functional and Surface Functionalized Glass, Alexander Dubcek University of Trencin, 91150, Slovakia*
[f] *Energy Materials and Devices (EMD) Laboratory, Department of Physics, National Institute of Technology, Warangal 506004, Telangana, India. E-mail: kanapuram.udaykumar@nitw.ac.in*

transition metals, multi-walled carbon nanotubes (MWCNTs) hold promise for facilitating and optimising the thermodynamics and kinetics of the hydrogen evolution reaction (HER).[9–11] This potential has led to the development of various CNT-based materials: namely, Pd-Ni@CNT and Ni-MoS@CNT, aimed at enhancing HER activity.[12,13] Metals with CNTs are recognised for their superior conductivity and stability and have been successfully integrated with transition metal composites (TMCs) to enhance their electro-catalytic properties for both the HER and oxygen evolution reaction (OER).[5] The synergetic effect between carbon nanomaterials and transition metals shows unique interfaces, fostering the creation of more exposed active sites and facilitating efficient electron transfer. This synergy is advantageous for improving the overall electrocatalytic performance towards water splitting applications. CNTs, with their exceptional electrical conductivity, mechanical strength, and large surface area, have proved to be excellent candidates for electrode materials in supercapacitors (SCs). Their unique one-dimensional structure allows for efficient electron transport and high specific capacitance. However, to address certain limitations such as their low specific capacitance and moderate conductivity, the integration of metal nanoparticles (NPs) onto CNT surfaces has been explored as a viable strategy.[14,15] A variety of metal NPs are included in the electrode materials of SCs, which are crucial to their functionality. Yet, their highly toxic nature and low stability impede widespread usage in practical device applications. Thus, the scientific and research community has switched attention to binary and ternary metals with CNTs due to the sluggish kinetics of electrons/ions between the electrode and the electrolyte. Unlike a single metal, metals with CNTs are promising electrode materials for SCs. The synergistic interaction of metal cations when applied with CNTs ensures better electrical conductivity. Moreover, metal NPs, owing to their high conductivity and unique catalytic properties, can significantly enhance the electrochemical performance of SCs. The hybridisation of CNTs with metal NPs not only facilitates improved charge storage but also contributes to enhanced redox reactions, resulting in a synergistic effect on their overall electrochemical performance.

The one-dimensional structure of CNTs facilitates efficient charge transfer, while their ability to adsorb a wide range of organic and inorganic species promotes their photocatalytic activity.[16,17] Inherent limitations, such as bandgap restrictions and recombination of photogenerated charges, can be effectively addressed by introducing metal NPs into the CNT framework. It is significant that metal NPs, renowned for their unique optical, electronic, and catalytic properties, contribute greatly to enhancing the photocatalytic performance of CNT-based composites. Synergistic effects arise from the ability of metal NPs to act as co-catalysts, promoting charge separation and surface reaction kinetics during photocatalysis.[18] Besides, the plasmonic properties of certain metal NPs can extend the absorption spectrum of the composite, enabling utilization of a broader range of sunlight for catalytic processes.[14,15] Recent studies have demonstrated that biomass-derived CNTs provide an even more sustainable pathway for pollutant remediation, offering enhanced performance while minimizing environmental impact. For example, CNTs synthesized from renewable biomass sources have shown excellent capability in removing heavy metals such as Pb^{2+}, Cd^{2+}, Cr^{6+}, and As^{3+} from contaminated water. CNTs offer a green, efficient, and scalable approach for detoxifying contaminated water, underscoring their growing relevance in eco-friendly remediation technologies.[19]

Transition metals incorporated with CNTs ensure excellent performance towards electrocatalytic and photocatalytic applications because of the availability of filled energy states, owing to multiple metal centres and the amelioration of the electrochemical and photocatalytic process. Silver (Ag), nickel (Ni), and copper (Cu) each contribute unique functional advantages that enhance the performance of hybrid materials in supercapacitors and photocatalysis. Ag offers superior electrical conductivity, high electron mobility, and strong plasmonic activity, which significantly improve charge-transfer kinetics and promote visible-light absorption for efficient catalytic reactions. Ni provides excellent redox activity through its Ni^{2+}/Ni^{3+} transitions, delivering high pseudo capacitance, good cycling stability, and enhanced charge separation in photocatalytic systems.[20] Cu, being earth-abundant and highly conductive, facilitates rapid electron transport and forms active Cu^{+}/Cu^{2+} species that strengthen both electrochemical and photocatalytic processes. Together, these metals create a synergistic effect that boosts conductivity, accelerates redox reactions, and enhances light-driven degradation efficiency.

This study presents a comprehensive investigation into recent advancements in the integration of carbon nanotubes (CNTs) with copper (Cu), silver (Ag), and nickel (Ni) nanoparticles (NPs), and bimetallic composites, focusing on their applications in the oxygen evolution reaction (OER), supercapacitors (SCs), and photocatalytic processes. The primary objective of this work is to develop an innovative and scalable approach for the functionalization of CNTs with diverse metal systems. We have successfully synthesized various metal-functionalized CNT composites through a facile chemical method, including monometallic systems (Ni, Cu, Ag), bimetallic combinations (Ni–Cu, Ni–Ag, Cu–Ag), and ternary systems (Ni–Cu–Ag). Functionalizing CNT surfaces with multiple metals significantly enhances their performance attributes by introducing synergistic properties such as tunable oxidation states, superior electrical conductivity, and adjustable optical band gaps. These modifications directly amplify the efficiency of key processes, including OER activity, specific capacitance, and the degradation of complex organic pollutants such as anti-inflammatories. To better understand the interactions between metal ions and the CNT framework, density functional theory (DFT) simulations have been employed. Comprehensive microstructural, surface chemical, and optical characterizations have also been conducted to unravel the fundamental properties driving the enhanced functionality of these novel composites. This work not only introduces a versatile strategy for multi-metal decoration on CNTs, but also lays the groundwork for future advancements in energy storage, catalysis, and environmental remediation technologies.

2. Materials and methods

2.1. Materials

All chemicals used are of high purity. Multi-walled carbon nanotubes (MWCNT type 5) (95%), silver nitrate ($AgNO_3$) (99.9%), copper(II) acetate ($Cu(CH_3COO)_2$) (98%), nickel chloride ($NiCl_2{\cdot}6H_2O$) (98%), and sodium borohydride ($NaBH_4$) (98%) were purchased from SRL Pvt Ltd, India. Polyvinylpyrrolidone (PVP) (99%), acetone (CH_3COCH_3) (99%) and ethanol (C_2H_5OH) (99.9%) were received from Nice Chemical Pvt Ltd, India. For the whole reaction, Millipore water was used.

2.2. Synthesis of MWCNTs with metal nanocomposites

Herein, a series of pristine metals were successfully synthesized with multi-walled carbon nanotubes (MWCNTs), encompassing binary metal systems such as Ni–Cu, Ni–Ag, and Cu–Ag, as well as a ternary metal system. The synthesis process commenced with the dispersion of 100 mg of MWCNTs in 50 mL of deionized (DI) water, facilitated by ultrasonication for 30 minutes to ensure uniform dispersion. Following this, metal precursors with a concentration of 0.2 M were introduced into the reaction mixture. To facilitate the reduction and stabilization of the metal nanoparticles, 1 g of sodium borohydride ($NaBH_4$) was employed as a reducing agent, and 1 g of polyvinylpyrrolidone (PVP) was added as a stabilizing agent. The mixture was then vigorously stirred for 1 hour to ensure homogeneity. Subsequently, the dark colloidal solution was transferred into a Teflon-lined stainless-steel autoclave and subjected to hydrothermal treatment at 180 °C for 24 hours in a hot air oven. After the autoclave was allowed to cool to room temperature, the resulting solution was collected and thoroughly washed with acetone, ethanol, and DI water to remove any unreacted precursors or impurities. The washed sample was then dried in a vacuum oven at 120 °C to obtain the final product.

The same synthesis protocol was meticulously followed to prepare binary and ternary metal nanocomposites (NCs) with MWCNTs, maintaining equal concentrations of the respective metal precursors. The synthesized samples were designated as K1, K2, K3, K4, K5, K6, and K7, corresponding to CNT–Ni, CNT–Cu, CNT–Ag, CNT–Ni–Cu, CNT–Ni–Ag, CNT–Cu–Ag, and CNT–Ni–Cu–Ag, respectively. This systematic approach ensures the reproducibility and scalability of the synthesis process, paving the way for further exploration of these advanced nanocomposites in various applications.

3. Results and discussion

3.1. Crystalline analysis

In Fig. 1, the X-ray diffraction (XRD) patterns of both binary and ternary carbon nanotubes (CNTs) functionalized with various metal nanoparticles (NPs), including Ag, Ni, and Cu, are presented. The analysis reveals characteristic diffraction peaks at 26.31° and 43.41°, which are indexed to the (002) and (100) lattice planes of CNTs, respectively, as confirmed by JCPDS No. 75-1621. Upon the incorporation of Ni NPs into the CNT matrix, additional diffraction peaks emerge at specific 2θ values, indicative of the crystalline nature of the metallic phase. These peaks exhibit notable shifts and variations in intensity, providing critical insights into the structural interactions and potential modifications within the CNT–Ni nanocomposites (NCs). Notably, two prominent peaks are observed at 45.99° and 51.41°, corresponding to the (111) and (200) crystallographic planes of face-centred cubic (FCC) Ni, respectively. These peaks serve as definitive markers for the presence of metallic Ni, as supported by ref. 21. The XRD results collectively highlight the successful integration of metal NPs into the CNT framework and offer a detailed understanding of the crystallographic changes induced by the functionalization process.

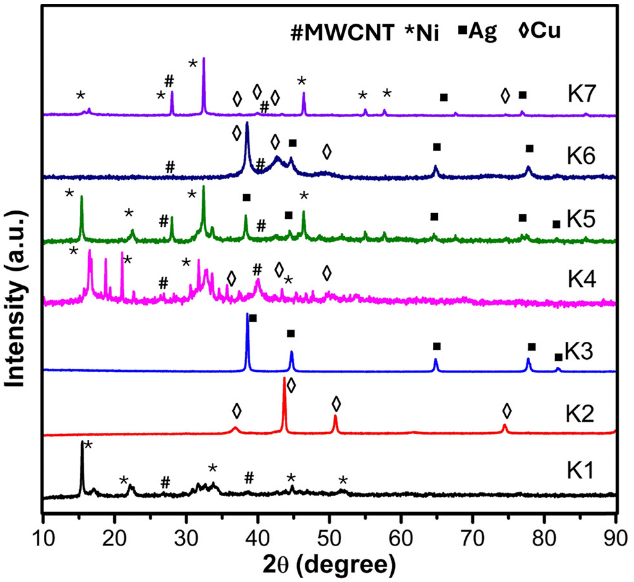

Fig. 1 X-ray diffraction spectra of the binary and ternary metal composites, K1 (CNT–Ni), K2 (CNT–Cu), K3 (CNT–Ag), K4 (CNT–Ni–Cu), K5 (CNT–Ni–Ag), K6 (CNT–Cu–Ag) and K7 (CNT–Ni–Cu–Ag nanocomposite).

For the CNT–Cu nanocomposites (NCs), the X-ray diffraction (XRD) patterns exhibit distinct peaks at various 2θ values, confirming the successful integration of Cu nanoparticles (NPs) into the CNT matrix. Notably, prominent diffraction peaks are observed at 43.76°, 50.95°, and 74.48°, which correspond to the (111), (200), and (220) crystallographic planes of face-centred cubic (FCC) Cu, respectively. The XRD analysis reveals an optimized spatial arrangement of Cu NPs on the CNT surface, which enhances the overall crystallinity and structural integrity of the composite. This improved crystalline ordering, particularly in the (111) and (200) planes, plays a pivotal role in augmenting the material's conductivity and catalytic efficiency. The precise alignment and orientation of Cu NPs, as elucidated by XRD, are critical for facilitating efficient electron transfer mechanisms, which are essential for enhancing performance in both electrochemical and photocatalytic applications. These

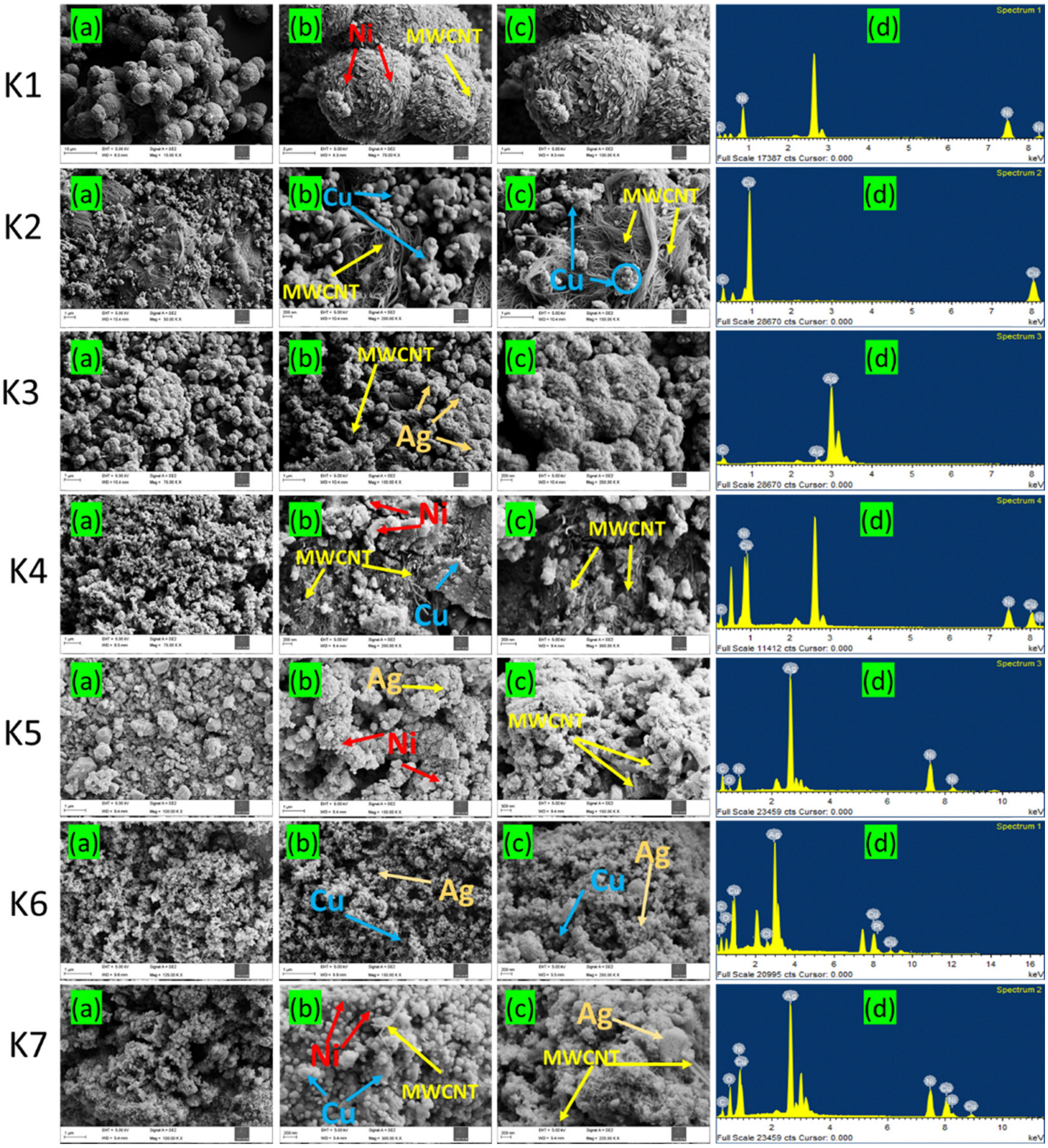

Fig. 2 FE-SEM images with different magnifications and corresponding EDS spectrum of K1 (a)–(d), K2 (a)–(d), K3 (a)–(d), K4 (a)–(d), K5 (a)–(d), K6 (a)–(d) and K7 (a)–(d).

findings underscore the importance of XRD in providing detailed insights into the structural and electronic modifications induced by Cu NP incorporation, ultimately contributing to the superior functional properties of the CNT–Cu NCs.

The XRD pattern of the CNT–Ag NC exhibited distinct peaks at specific 2θ values, signifying the crystalline nature of CNT–Ag NC. Peaks at 38.41°, 44.83°, 65.16°, and 77.83° are noted, corresponding to the (111), (200), (220), and (311) crystallographic planes of FCC Ag, respectively. These peaks, characteristic of the metallic Ag, confirm the successful integration of Ag NPs on the CNT surface.[21]

It is noted that XRD analysis of the bimetallic CNT NCs (CNT–Ag–Cu, CNT–Ni–Cu, CNT–Ni–Ag) demonstrates characteristic peaks, corresponding to the crystalline phases of both metal NPs and CNTs. The distinctive peaks at specific 2θ values provide information about the crystallographic planes of the integrated metals. The crystallinity and phase purity of the NCs, as confirmed, establish the foundation for understanding their structural integrity. This information is crucial to achieve the desired properties, such as catalytic activity or electrical conductivity. Tuning the NCs based on XRD data can enhance their catalytic properties, making them promising candidates for application in water splitting, energy storage and photocatalytic applications.[22]

3.2. Morphological analysis

To examine the surface morphology and elemental composition of the synthesized CNT–metal nanocomposites (NCs), field emission scanning electron microscopy (FE-SEM) and energy-dispersive X-ray spectroscopy (EDS) were employed. As illustrated in Fig. 2K1(a)–(c), the micrographs at different magnifications reveal a uniform distribution of Ni nanoparticles

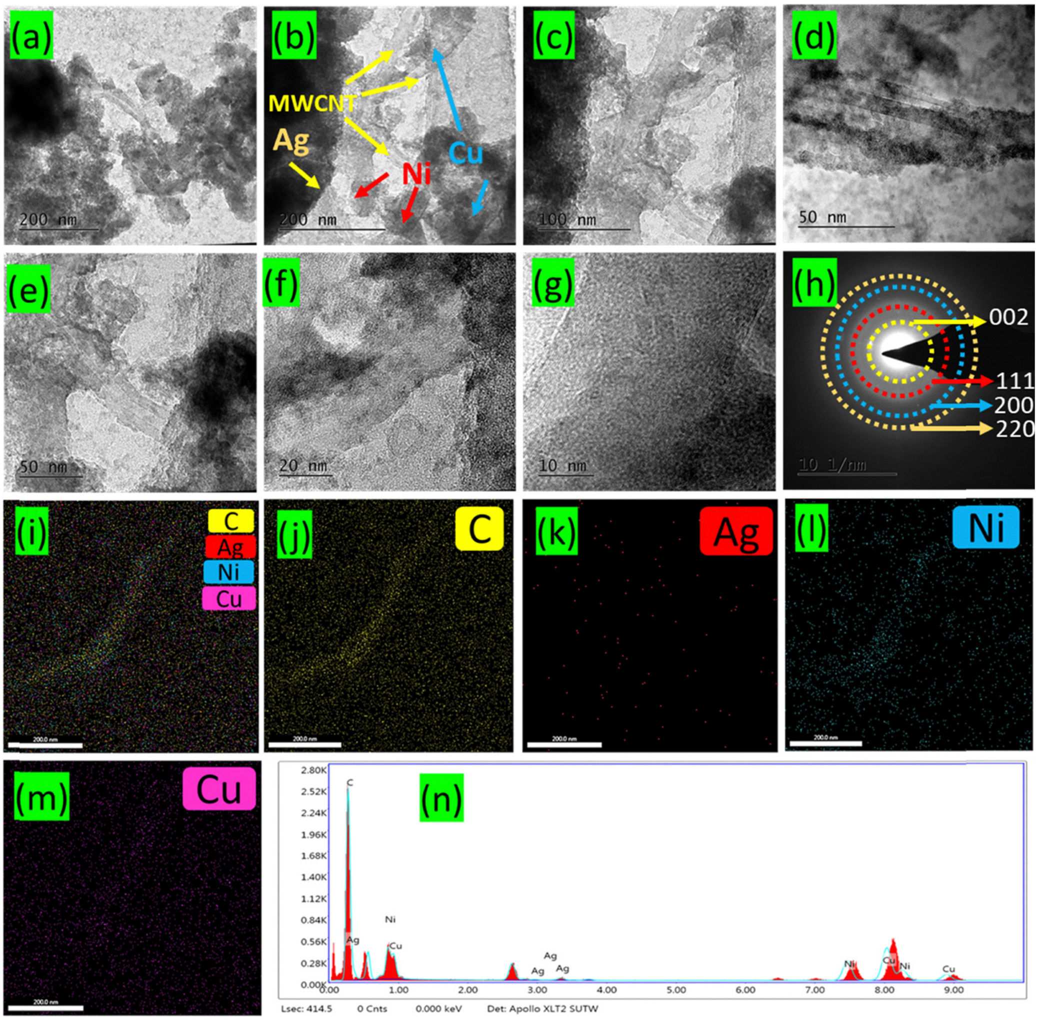

Fig. 3 (a)–(g) HR-TEM images of CNT–Ni–Cu–Ag with different magnifications, (h) the corresponding SAED pattern, (i)–(m) the corresponding elemental mapping images and (n) EDS spectrum of the CNT–Ni–Cu–Ag nanocomposites.

(NPs) across the CNT surface. The self-assembly of the Ni metal with CNTs during the chemical synthesis led to the formation of distinct microsphere structures. Higher magnification images indicate that these microspheres consist of interconnected thin Ni flakes, demonstrating a homogeneous attachment supported by the CNT matrix.[23] In Fig. 2K1(d), EDS analysis confirms the elemental composition of the K1 sample, indicating the presence of carbon (C) from CNTs and nickel (Ni). Similarly, Fig. 2K2(a)–(c) depicts the FE-SEM analysis of the CNT–Cu NCs, showcasing well-defined morphologies with Cu nanospheres uniformly dispersed on the CNT surface. The CNTs exhibit a characteristic tubular structure with a uniform diameter distribution, where individual nanotubes are clearly visible, often forming bundles due to strong van der Waals interactions. The CNTs appear twisted and entangled, creating large aggregated bundles. The Cu NPs are predominantly spherical, evenly dispersed throughout the sample, and exhibit smooth, densely packed surfaces around the CNTs. EDS analysis, as shown in Fig. 2K2(d) confirms the presence of both carbon (C) and copper (Cu) elements within the composite, further validating the successful integration of Cu NPs on the CNT framework.[24] In Fig. 2K3(a)–(c), the FESEM images of CNTs with Ag NPs are shown. The micrographs clearly reveal a spherical morphology, consistent with the formation of a composite structure with CNTs. Some Ag metal NPs are observed to agglomerate, forming small clusters on the surface of the CNTs. The CNTs are uniformly distributed throughout the silver matrix, and to a large degree, the innovative wet mixing technique has prevented CNT aggregation. Nonetheless, in the CNT–Ag NCs, several CNT clusters are discernible. In Fig. 2K3(d), EDS analysis verifies the presence of both C and Ag.[25] FESEM analysis of the K4 to K6 NCs, as presented in Fig. 2K4–K6(a)–(c), reveals a similar morphology of the CNTs with the distribution of different Ni, Cu and Ag metal NPs. This similarity might be due to the spherical and tubular morphology of the CNT, Ni, Cu and Ag clusters. In the case of CNT–Ni–Cu–Ag NCs depicted in Fig. 2K7(a)–(c), a large number of small Ni–Cu–Ag metal NPs are observed, forming clusters of homogeneous sizes that densely cover the CNTs. This packed arrangement suggests strong interaction between the metal

NPs and the CNTs, which potentially enhances the composite's properties.[26]

EDS analysis of the K4–K7 NCs in Fig. 2d affirms the presence of C, Ni, Cu and Ag elements, without any impurities. Modification of the CNTs with various noble metals offers different applications. Besides, metal-decorated CNT NCs can further enhance surface area and conductivity.[23] In Fig. 3(a)–(m), a detailed high-resolution transmission electron microscopy (HR-TEM) analysis of the novel NCs comprising CNTs decorated with Ni, Cu and Ag metal NPs (K7) is given. In Fig. 3(a)–(g), it is observed that the various metal NPs are attached tightly onto the CNT surface.[23] The metal NPs exhibit a spherical morphology and a consistent diameter of around 5 nm. They are uniformly disseminated without agglomeration and firmly attached to the surface of the MWCNTs. This outcome proves that the metal NPs have been uniformly decorated onto the surface of the CNTs.[24]

3.3. UV-Vis analysis

UV-Vis spectroscopy was employed to analyse the optical properties of the samples K1 to K7. Fig. S1(a) and (b) present the absorption spectra and band gap plots of the metal-incorporated carbon nanotube (CNT) nanocomposites (NCs). The spectra were recorded across a wavelength range of 200 to 1000 nm under ambient conditions. All samples (K1 to K7) demonstrate significant light absorption in the UV and UV-Vis regions. The distinct optical features observed in the UV spectra can be attributed to the synergistic contributions of the CNTs and metal nanoparticles (NPs).[27] CNTs typically exhibit characteristic absorption peaks in the UV region, arising from π–π* transitions in their sp^2-hybridized carbon structure. Meanwhile, the incorporation of metal NPs introduces plasmonic resonances, which further enhance the overall absorption in the UV range. Notably, metal NPs, particularly silver (Ag), exhibit strong surface plasmon resonance (SPR) in the UV region, leading to well-defined peaks in the spectra. These SPR effects contribute to enhanced optical absorption and scattering properties. Among the prepared samples, K7 (CNT–Ni–Cu–Ag) demonstrates superior optical activity, outperforming the other CNT-based NCs.[22] This enhanced performance is likely due to the combined effects of the plasmonic properties of Ag, the catalytic activity of Ni and Cu, and the structural advantages of CNTs, making K7 a highly promising material for optoelectronic and photocatalytic applications.

3.4. FT-IR analysis

Fourier transform infrared absorption (FT-IR) analysis was used to locate the functional groups present in the synthesized samples. In Fig. S2, the FT-IR spectra of the K1 to K7 (CNT–Ni, CNT–Cu, CNT–Ag, CNT–Ni–Cu, CNT–Ni–Ag, CNT–Cu–Ag and CNT–Ni–Cu–Ag) samples are illustrated. In Fig. S2a, due to the O–H stretching vibration, a broad peak centred around 3295 cm^{-1} occurred. Peaks at 1650 to 1550 cm^{-1} signify C–C bond stretching while the peak at 1176 cm^{-1} is assigned to the C–O stretching vibration. The above functional groups present in the FT-IR spectrum indicate the CNT structure.[28] Furthermore, peaks at 973 and 459 cm^{-1} can be attributed to the presence of Ni on the surface of the CNTs. In Fig. S2b, the K2 spectrum is similar to the K1 spectrum with some peaks coinciding at 3666 cm^{-1}, representing the O–H stretching vibration. Another peak seen at 910 cm^{-1} belongs to the C–H bond. The peak at 1100 cm^{-1} is attributed to the C–O stretching vibration of the ether groups. Furthermore the peak at 640 cm^{-1} is due to Cu, which denotes the presence of Cu on the CNT surface. In Fig. S2c, the K3 spectrum is similar to the K1 spectrum, but with a broader peak at around 3147 cm^{-1} representing the carboxyl groups. This broader peak is due to the overlapping of the O–H stretching vibration. The peak at 1712 cm^{-1} is attributed to the C═O stretching vibration of the carbonyl groups. The shift can be due to the presence of Ag metal on the surface of the CNTs. This shift can also be observed at 1226 cm^{-1} and 867 cm^{-1} of the C–H bond.

In Fig. S2d, the K4 spectrum is represented at 3344 cm^{-1}, a relatively sharp peak which is assigned to the O–H stretching vibration.[29] The peak located at 1618 cm^{-1} denotes C–C bond stretching, and the peak at 1230 cm^{-1} belongs to the C═O bond. Peaks observed at 935 cm^{-1}, 445 cm^{-1} and 1405 cm^{-1}, and 760 cm^{-1} could be due to Ni and Cu, respectively.[30] In Fig. S2e, the K5 spectrum is a combination of the K1 and K3 spectra. In the K5 spectrum, the peak at 3286 cm^{-1} is due to the O–H vibration mode, while the peak at 1608 cm^{-1} is due to the C–C bond stretching vibration. All other peaks are like K1 and K3 with minor shifting owing to the presence of both Ni and Ag. The K6 spectrum highlights characteristic peaks of K2 and K3. As such, the broad peaks at 937 cm^{-1} and 746 cm^{-1} are attributed to the presence of mixer phases of Cu and Ag, as denoted in Fig. S2f. The K7 spectrum is akin to K6 with similar major peaks. However, the broad peaks at 3200 cm^{-1} to 2880 cm^{-1} present in K6 have been suppressed as a result of the presence of Ni, Cu and Ag.[27]

3.5. Raman analysis

In Fig. S3, the Raman spectra of CNTs decorated with K1–K7 metal compositions are shown. The D band in the Raman spectrum can be used to estimate the number of defects. Two distinct peaks between 1320 and 1600 cm^{-1} are identified in the CNT (K1 to K7 sample) NCs. The D band is caused by defects and lattice mismatches. In contrast, the G band is caused by the E_{2g} mode, which involves stretching vibrations of sp^2 linked C–C bonds. In particular, the D band originates from the first-order scattering process of sp^3 carbon caused by the presence of in-plane substitutional heteroatoms, vacancies, grain boundaries, or other defects, as well as finite size effects; all of these reduce the crystalline symmetry of the quasi-infinite lattice.[31,32] The G band reflects the sp^2 carbon states associated with the graphitic hexagon-pinch mode.[33] Studies carried out about Raman spectra for CNTs (K1–K7 samples) show that the number of defects in the graphene layers depends on the ratio of I_D/I_G, which is tabulated and shown in Table S1. Accordingly, for the Raman spectra: CNT–Ni, CNT–Cu, CNT–Ag, CNT–Ni–Cu, CNT–Ni–Ag, and CNT–Ni–Cu–Ag, the ratio I_D/I_G corresponded to 0.20, 0.10, 0.74, 0.92, 0.56, and 1.07, respectively. It is seen that the CNT–Ni and CNT–Cu samples have high purity. As for CNT–Ni–Cu and CNT–Ni–Cu–Ag, the ratio I_D/I_G decreased. However, the ratio I_D/I_G of CNT–Ni–Cu–Ag ($I_D/I_G \sim 1.07$) significantly increased. It is noted that the D band intensity increased with decreasing CNT content.[31,32] This phenomenon can be attributed to the accumulation of carbonaceous by-products on the surface. Additionally, as the mass percentage of CNTs decreases, the intensity of the G band in the Raman spectrum increases. This is likely due to the relative enhancement of graphitic characteristics in the remaining carbon structure, as the contribution from CNTs diminishes. The G band, which corresponds to the in-plane vibrational mode of sp^2-hybridized carbon atoms, becomes more pronounced in the absence of the distinct structural features of CNTs, reflecting a shift in the carbon phase composition.

3.6. Surface chemistry investigations

To investigate the chemical composition and oxidation states of the CNT-based composites (K4, K5, K6, and K7), X-ray photoelectron spectroscopy (XPS) analysis was used. In Fig. S4(a)–(e), the K4 NC core level high-resolution spectrum and survey spectra are illustrated. As observed, the binding energy associated with 933 and 953 eV in the Cu high-resolution spectra corresponds to 2p3/2 and 2p1/2, respectively.[34] Satellite peaks located at 942 eV and 961 eV indicate the presence of copper oxides (CuO) in the NC. This finding could be due to surface exposure, which causes mild oxidation of the Cu matrix.[35] The high-resolution C 1s spectra of K4 demonstrate peaks due to carbon sp^2 and sp^3 hybridization. The spectra signify that the percentage of sp^2 hybridization carbon is larger than the percentage of sp^3 hybridization carbon, indicating that the composite has a higher degree of graphitization with fewer lattice defects.[36,37] The prominent C 1s signal for sp^2 carbon, which is also found in other composites, denotes that the conjugated bonds in CNT are preserved even in composite form.[38] It is seen that when Ni is incorporated in the composite, the C 1s peak becomes more asymmetric owing to the creation of a shoulder peak at higher binding energies.[39] At around 287 eV, a C–OH peak appeared, which is due to the absorption of water molecules. In Fig. S4, the high-resolution spectra of Ni 2p, with peaks at 855.2 eV and 872.7 eV, are ascribed to 2p3/2 and 2p1/2, respectively. Such an outcome indicates that Ni is present in the composite as Ni^{2+}.[40] There is no apparent peak associated with metallic Ni around 852 eV, indicating that Ni NPs on the CNT surface give good capacitance properties.[41] Furthermore, satellite peaks are observed at around 860 eV and 880 eV that have a higher binding energy than peaks assigned to Ni^{2+}.[42]

In Fig. S5(a)–(e), XPS survey spectra along with high-resolution spectra of the elements Ni, Ag, C, and O are seen to be present in K5 NC. The binding energy values of 367 eV and 373 eV in the Ag 3d spectra are related to 3d5/2 and 3d3/2, respectively: no further peaks are identified. This binding energy value shows that the silver included in the composite has been oxidised. Ni 2p high-resolution spectra in K5 NC exhibit a similar pattern to K4 NC. However, in the case of K6 NC (Fig. S6(a)–(e)), additional peaks arise at 367.4 eV and 372.4 eV, which correspond to silver peaks (Ag_2O and AgO).[43] In ultra-high vacuum, however, AgO is found to be unstable, and its existence cannot be verified.[44] Peaks located at 368 eV and 373.8 eV are ascribed to metallic Ag, which indicates that CNT is effective as a protective layer in this composite, preventing the oxidation of Ag NPs.[45] This pattern was not seen in other composites. In Fig. 4(a)–(f), the existence of Ni, Cu, Ag, C,

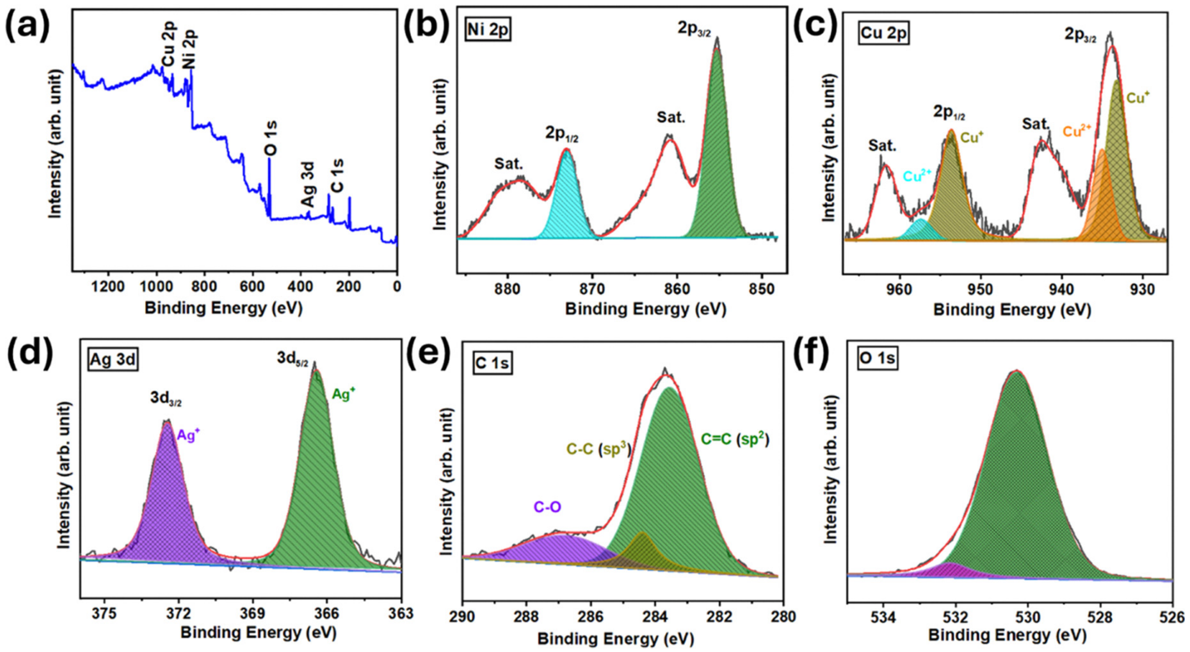

Fig. 4 (a) XPS survey spectrum of CNT–Ni–Cu–Ag (K7), and (b)–(f) high-resolution spectra of Ni 2p, Cu 2p, Ag 3d, C 1s and O 1s, respectively.

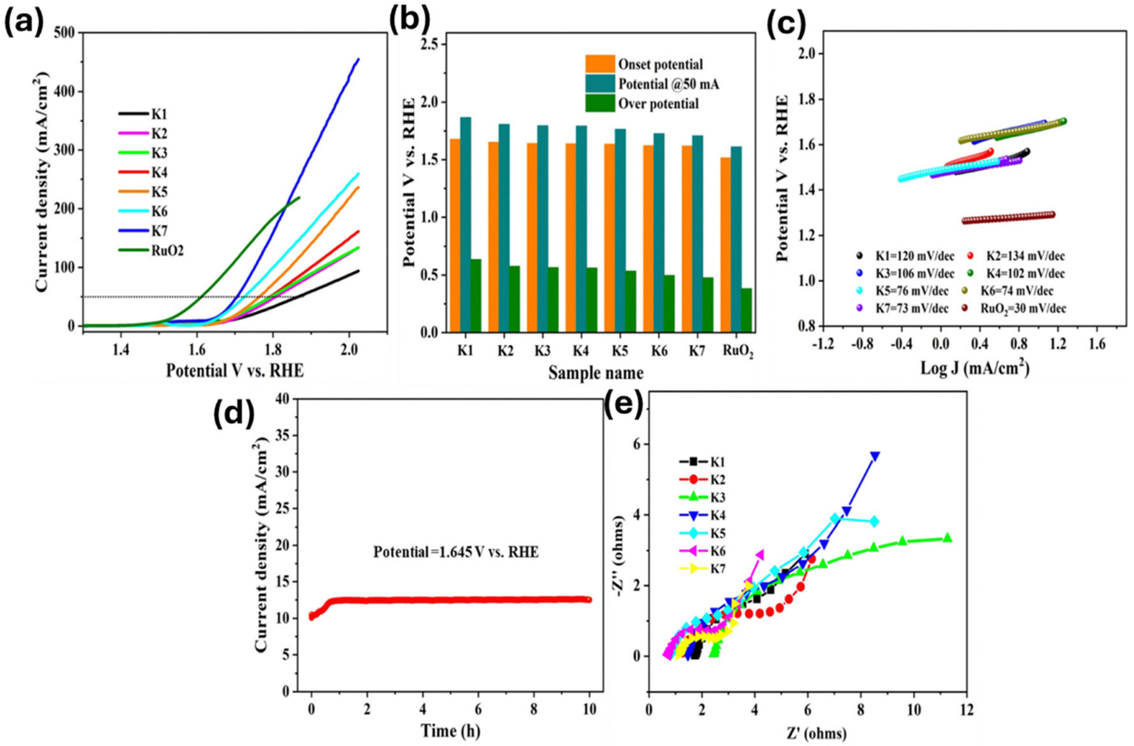

Fig. 5 OER analysis using 1 M KOH: (a) polarization curves of K1–K7 and RuO_2. (b) Comparison of onset potential, the potential required to reach 50 mA cm^{-2} current density, and overpotential for K1–K7 and RuO_2. (c) Corresponding Tafel slopes. (d) Chronoamperometry analysis of K7, and (e) EIS analysis of K1–K7 NPs.

and O elements is seen. The presence of copper in the +1 and +2 oxidation states is confirmed by the presence of peaks at 933 eV and 935 eV. The high intensity of sp^2 hybridization signifies that CNTs have a high degree of graphitization and fewer lattice defects. A tiny peak on the higher binding energy side of the O 1s spectra confirms the presence of Ag–O bonding. In Table S2, the binding energies of C, O, Ni, Cu and Ag elements for the K4–K7 samples are given.

3.7. OER analysis

Using 1 M KOH as an electrolyte solution, the synthesized metal and metal-based-NCs (K1 to K7) were applied for OER activities. In Fig. 5, the results are shown. In Fig. 5a, the linear sweep voltammetry (LSV) curves of K1 to K7 and RuO_2 NPs are depicted. Hence, the onset potential values: K1 (1.6772 V), K2 (1.6504 V), K3 (1.6406 V), K4 (1.6376 V), K5 (1.6212 V), K6 (1.6187 V) and K7 (1.516 V) *vs.* RHE are observed. It is noted that the current density of K7 NC reached about 450 mA cm^{-2}, which is relatively higher compared with that of other metal and metal-based NCs. Furthermore, the potential of 50 mA cm^{-2} is observed at 1.8653 V, 1.8064 V, 1.7948 V, 1.7921 V, 1.7650 V, 1.7260 V, 1.7065 V and 1.612 V *vs.* RHE, for K1, K2, K3, K4, K5, K6 and K7 NCs, respectively.

It is acknowledged that overpotential is one of the key parameters that determines an electrocatalyst's OER performance. As a reference standard for OER performance, 50 mA cm^{-2} is commonly utilised. Hence, the lower overpotential of the NCs indicates stronger OER reactivity. Of all samples, K7 NC exhibited the best OER activity, as demonstrated by the lowest overpotential of 382 mV at 50 mA cm^{-2} (Fig. 5b). In Fig. 5b, a comparison of reaction performance, overpotentials, and catalytic current density at 50 mA cm^{-2} is seen. The overpotential of K7 NCs (382 mV cm^{-2}) was found to be much smaller than the other samples: K1 (635 mV cm^{-2}), K2 (576 mV cm^{-2}), K3 (564 mV cm^{-2}), K4 (562 mV cm^{-2}), K5 (535 mV cm^{-2}), K6 (496 mV cm^{-2}) and reference sample of RuO_2 (382 mV cm^{-2}).

Furthermore, in Fig. 5c, the Tafel plots of K1–K7 and RuO_2 are displayed. Thus, the Tafel slope values of K1–K7 and RuO_2 proved to be about 120 mV dec^{-1}, 134 mV dec^{-1}, 106 mV dec^{-1}, 102 mV dec^{-1}, 76 mV dec^{-1}, 74 mV dec^{-1}, 73 mV dec^{-1} and 30 mV dec^{-1}. It is seen that the K7 NCs revealed the lowest Tafel slope value compared with samples K1–K6. Such an outcome shows that K7 possesses better OER activity in an alkaline medium. In addition, the material stability of the K7 NCs was evaluated *via* chronoamperometric analysis, over a period of 10 h. As a result, the K7 electrode demonstrated a stable current density of about 12 mA cm^{-2} for the potential of 1.645 V *vs.* RHE (Fig. 5d). In Fig. 5e, Nyquist plots of the samples are presented. Accordingly, the charge transfer resistance (R_{ct}) of the metal and metal-based NCs for K1, K2, K3, K4, K5, K6 and K7 is seen to correspond to 2.33 Ω, 3.3 Ω, 8.76 Ω, 6.2 Ω, 4.33 Ω, 1.69 Ω and 1.49 Ω, respectively. The K7 NCs possessed the lowest R_{ct} of 1.49 Ω, which confirms the high charge transfer during OER analysis.

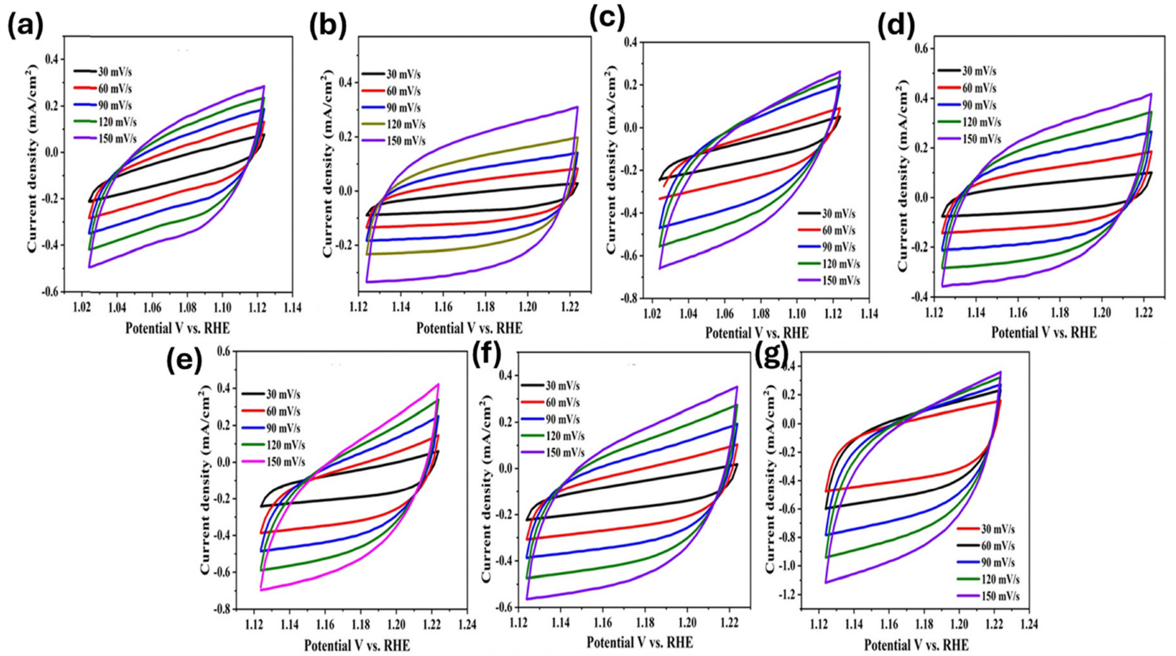

Fig. 6 (a)–(g) CV analysis of the electrodes: K1 as CNT–Ni, K2 as CNT–Cu, K3 as CNT–Ag, K4 as CNT–Ni–Cu, K5 as CNT–Ni–Ag, K6 as CNT–Cu–Ag and K7 as CNT–Ni–Cu–Ag, at different scan rates.

The electrochemically active surface area (ECSA) of the K1–K7 NCs was analysed through cyclic voltammetry (CV) analysis. ESCA is directly proportional to the electrochemical double-layer capacitance (C_{dl}) of the NCs. To determine C_{dl}, CV analysis was carried out at various scan rates (Fig. 6a–g). The current density (ΔJ) was calculated as the difference between the anodic and cathodic peak current density ($J_{\mathrm{a}} - J_{\mathrm{c}}$). The plots of scan rate *vs.* current density provide information regards NCs C_{dl}. In Fig. S7(a)–(g), the calculated C_{dl} values of the K1–K7 are presented. Hence, the C_{dl} values for K1–K7 proved to be 2.5 μF cm^{-2}, 2.6 μF cm^{-2}, 2.8 μF cm^{-2}, 2.8 μF cm^{-2}, 3.1 μF cm^{-2}, 3.2 μF cm^{-2} and 3.2 μF cm^{-2}, respectively. The K7 NCs reveal the highest C_{dl} value, demonstrating enhanced OER activity in the alkaline medium. It is evident, therefore, that the K7 NCs can perform well in an alkaline medium. The combination of enhanced charge transport increased active sites, redox behaviour, and synergistic interactions between CNTs and metal nanoparticles (Ag, Cu, Ni), significantly boosting the OER performance. These properties make metal-decorated CNTs highly efficient and durable catalysts for renewable energy applications, such as water splitting and fuel cells.

3.8. Supercapacitive analysis

To further understand the electrochemical charge storage behaviour of metal NCs with CNTs, K1 (CNT–Ni), K2 (CNT–Cu), K3 (CNT–Ag), K4 (CNT–Ni–Cu), K5 (CNT–Ni–Ag), K6 (CNT–Cu–Ag) and K7 (CNT–Ni–Cu–Ag) electrodes were characterized *via* CV, GCD and EIS. In Fig. 7, the detailed supercapacitor performance of each sample is displayed. The CV curves at different scan rates (5–100 mV s^{-1}) under a fixed potential window (0.0–0.6 V) were obtained.[46]

In Fig. 7a, the CV curves show a faradaic pattern with a non-rectangular shape. In each curve, there is a pair of redox peaks, which may be associated to the pseudocapacitance characteristic of the K1 (CNT–Ni) electrode, using 6 M KOH electrolyte. As the scan rates increased, the redox peaks consistently maintained their integrity, indicating excellent rate performance. In Fig. 7b, the CV curves of the K2 (CNT–Cu) electrode are recorded at various scan rates in the same potential window.[47] All CV curves show well-defined reversible redox peaks, indicating typical pseudocapacitive behavior. In Fig. 7c, the CV curves of the K3 (CNT–Ag) electrode at various scan rates are displayed.[48] In the K3 electrode, oxidation/reduction peaks are observed at lower scan rates. As such, this outcome indicates that the K3 electrode is storing charge in a faradaic manner. Furthermore, as the scan rate increases, the CV curves become broader and the redox peaks are seen to shift slightly. In Fig. 7d, the CV curves of the K4 (CNT–Ni–Cu) electrode at different scan rates are shown.[49,50] The CV profile of the double metal electrode contains redox peaks, showing pseudocapacitive behaviour due to the faradaic mechanism, which is caused by the interaction of hydroxyl ions in the KOH electrolyte along with the bi-metal of the Ni–Cu electrode. As the scan rates increased, the redox peak intensities increased, scarcely shifting towards a higher potential, indicating that fast redox reactions occur at the interface between the active material and the electrolyte.

In Fig. 7(e) and (f), the electrochemical performance of the binary-based CNT–Ni–Ag and CNT–Cu–Ag electrodes was observed. Due to the presence of Ag metal, the CV curves

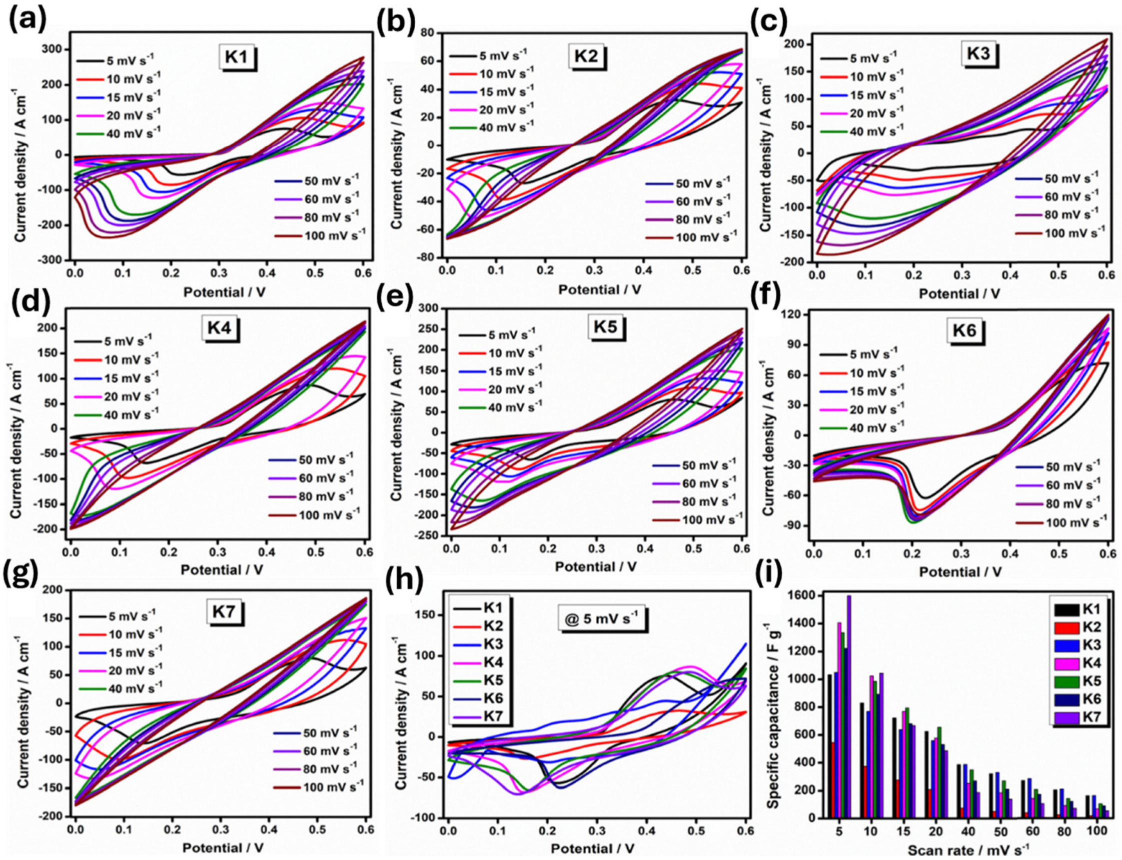

Fig. 7 Electrochemical analysis: (a)–(g) CV curves represent the fabricated CNT–metal based electrodes (K1 to K7) measured at various scan rates. (h) Comparative CV curves of the K1 to K7 electrodes, respectively, and (i) obtained specific capacitance, at different scan rates.

showed additional redox active sites, which enhance the electrochemical performance.[51] In Fig. 7g, the CV curves of the ternary-metal composed with CNT (K7) electrode, at 0.0–0.6 V potential window, are displayed. As scan rate increased, the total current density increased in the CV plots, revealing a diffusion-controlled phenomenon, which is a slow process. The size of the diffusion layer above the electrode surface also varied, according to the voltage scan rate. Higher scan rates cause a smaller differential between the diffusion layer and the surface of the electrode surface, resulting in enhanced flux to the electrode surface. As a result, the current accelerated. When the scan rates increased further, the redox peaks shifted slightly, resulting in increased peak separation. Peak separation is due to solution resistance plus the significant effect of the *iR* drop.[52] Owing to its large surface area, Ni–Cu–Ag acts as a supporting material for the CNT electrode. Hence, better intercalation and deintercalation of the electrolyte ions are seen, generating greater specific capacitance values.

In Fig. 7h, the comparative CV curves of all these electrodes at a scan rate of 5 mV s^{-1} are shown. The redox peaks reveal pseudocapacitive behaviour caused by the faradaic mechanism, arising from electrolyte contact with the corresponding electrode. As the scan rates increased, the redox peak intensities increased, shifting slightly towards a higher potential. It is noted that rapid redox reactions occur at the active material-electrolyte interface. In Fig. 7i, the maximum specific capacitance, calculated from the CV plots, proved to be 1033 F g^{-1}, 545 F g^{-1}, 1050 F g^{-1}, 1406 F g^{-1}, 1334 F g^{-1}, 1224 F g^{-1} and 1600 F g^{-1} for the K1, K2, K3, K4, K5, K6 and K7 electrodes at 5 mV s^{-1}, respectively. The high specific capacitance of the K7 (CNT–Ni–Cu–Ag) electrode denotes the synergistic interaction between the CNT and metal surfaces.[53] The diffusion kinetics of the electrodes were further calculated using the Randles–Sevcik equation as shown in Fig. S10. The CNT–Ni–Cu–Ag electrode records an apparent diffusion coefficient of 2.27×10^{-7} cm^2 s^{-1}, which is somewhat lower than that observed for the binary composites (CNT–Ni–Cu and CNT–Cu–Ag). This outcome implies that introducing all three metals together creates additional structural or interfacial complexities that slightly slow down ion transport compared to the simpler binary systems. Even so, the CV profiles reveal sharp and nearly symmetric anodic and cathodic peaks, confirming that the electrode maintains balanced and reversible redox activity. Overall, the CNT–Ni–Cu–Ag composite demonstrates stable charge transfer kinetics, combining moderate ion diffusion with a well-defined and symmetric electrochemical response, despite its diffusion rate being marginally reduced relative to certain binary counterparts.

In Fig. 8, all the GCD curves present a sloping trend, which is consistent with the CV results. In Fig. 8(a) and (b), the GCD

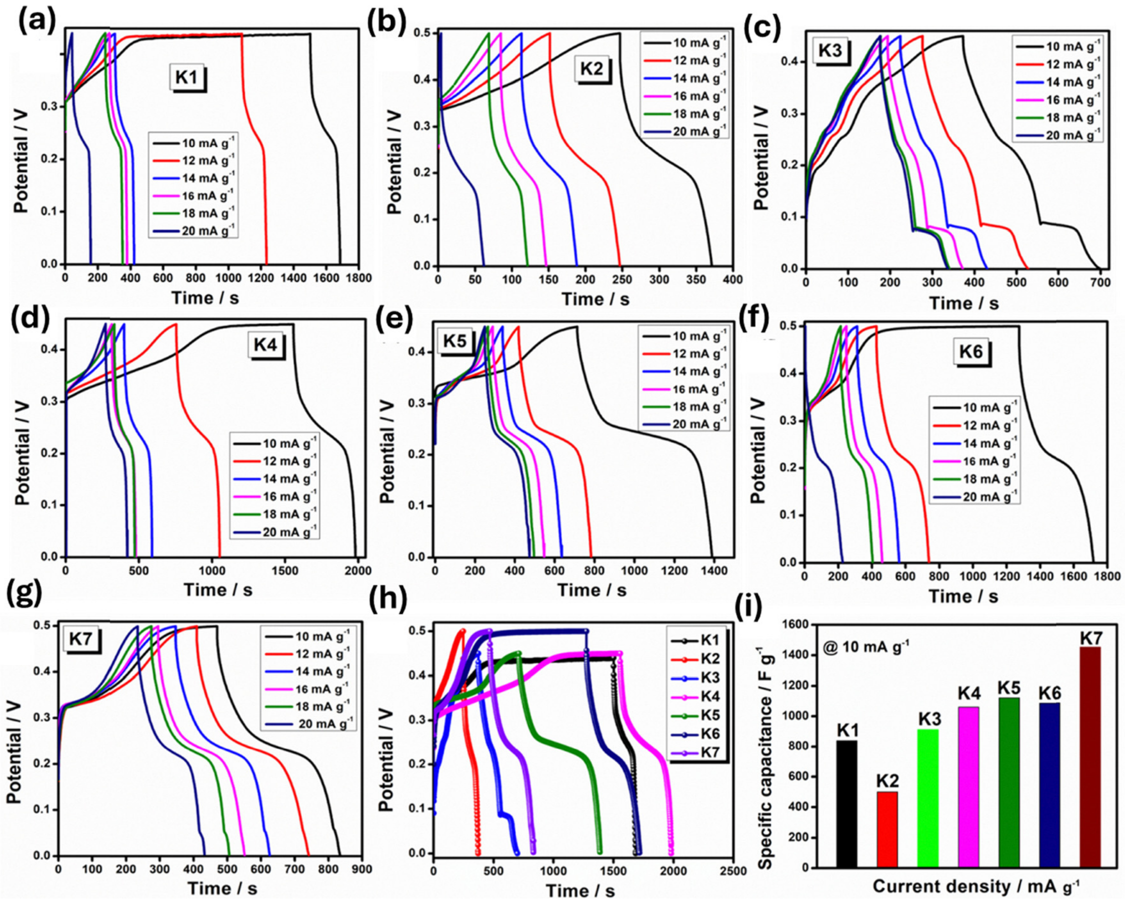

Fig. 8 Electrochemical measurements: (a)–(g) GCD curves of the fabricated electrodes (K1 to K7) measured at various scan rates. (h) Comparative GCD curves of the K1 to K7 electrodes, respectively, and (i) obtained specific capacitance at 10 mA g^{-1} current density.

curves at different current densities are illustrated. This electrode demonstrated typical pseudocapacitive behaviour with non-linear discharge curves. This behaviour has also been observed in the GCD curves at different current densities (Fig. 8c). Furthermore, when Ag is combined with CNTs, the overall GCD curve profile changes.[54] Thus, the presence of CNTs with metallic Ni and Cu contributed to a higher current density in the GCD profile, as denoted in Fig. 8d. The metals, functioning as a current collector, can reduce resistance and improve the conductivity of the CNT–Ni–Cu electrode. In Fig. 8(e) and (f), the GCD curves of the K1–K7 samples at various current densities are displayed. All GCD curves are triangle-shaped with strong symmetry, indicating that each sample has good charge–discharge reversibility. In Fig. 8g, the nonlinear GCD plots indicate their divergence from ideal character. Specific capacitance is mostly contributed by the redox process. In Fig. 8h, the comparative GCD curves and the corresponding capacitance value are summarised, as shown in the bar diagram in Fig. 8i. Herein, the maximum specific capacitance obtained for the K1, K2, K3, K4, K5, K6 and K7 electrodes is found to be 838 F g^{-1}, 500 F g^{-1}, 912 F g^{-1}, 1085 F g^{-1}, 1116 F g^{-1}, 1086 F g^{-1} and 1451 F g^{-1}, respectively. The specific capacitance obtained in the present study was compared to prior reported work; the results are summarised in Table S3.[46,48,49,51–67] The specific capacitance decreased linearly with increasing current due to the speedy attainment of the operational voltage range at high current, resulting in rapid charge–discharge. All the GCD graphs revealed the pseudocapacitive nature of the electrodes.

To better understand the charge transfer mechanism and calculate the resistance associated with charge storage at the electrode/electrolyte contact, EIS was implemented. In Fig. S8a, the EIS-Nyquist plots of the K1–K7 samples, in the frequency range of 100 kHz to 0.01 Hz, are observed. The AC impedance spectra of the samples K5 and K6 are represented *via* Nyquist plots at a frequency of 100 kHz to 0.01 Hz.[65] Electrochemical performance is seen to be higher for the K7 (CNT–Ni–Cu–Ag) electrode. In Fig. S8b, the cycling stability of the K7 (CNT–Ni–Cu–Ag) electrode at a current density of 15 mA g^{-1} is presented. The capacitance retention of the K7 electrode shows a higher cyclic stability of 99%@5000 cycles compared with other electrodes reported elsewhere.[66,67] In Fig. S9, the electrochemical mechanism of the K7 electrode is depicted. The metals incorporated on the CNT surface exhibited high specific capacitance due to a combination of factors that enhance their electrochemical performance including increased surface area, improved electrical conductivity, pseudocapacitance contribution, synergistic effects at the metal–CNT interface, enhanced

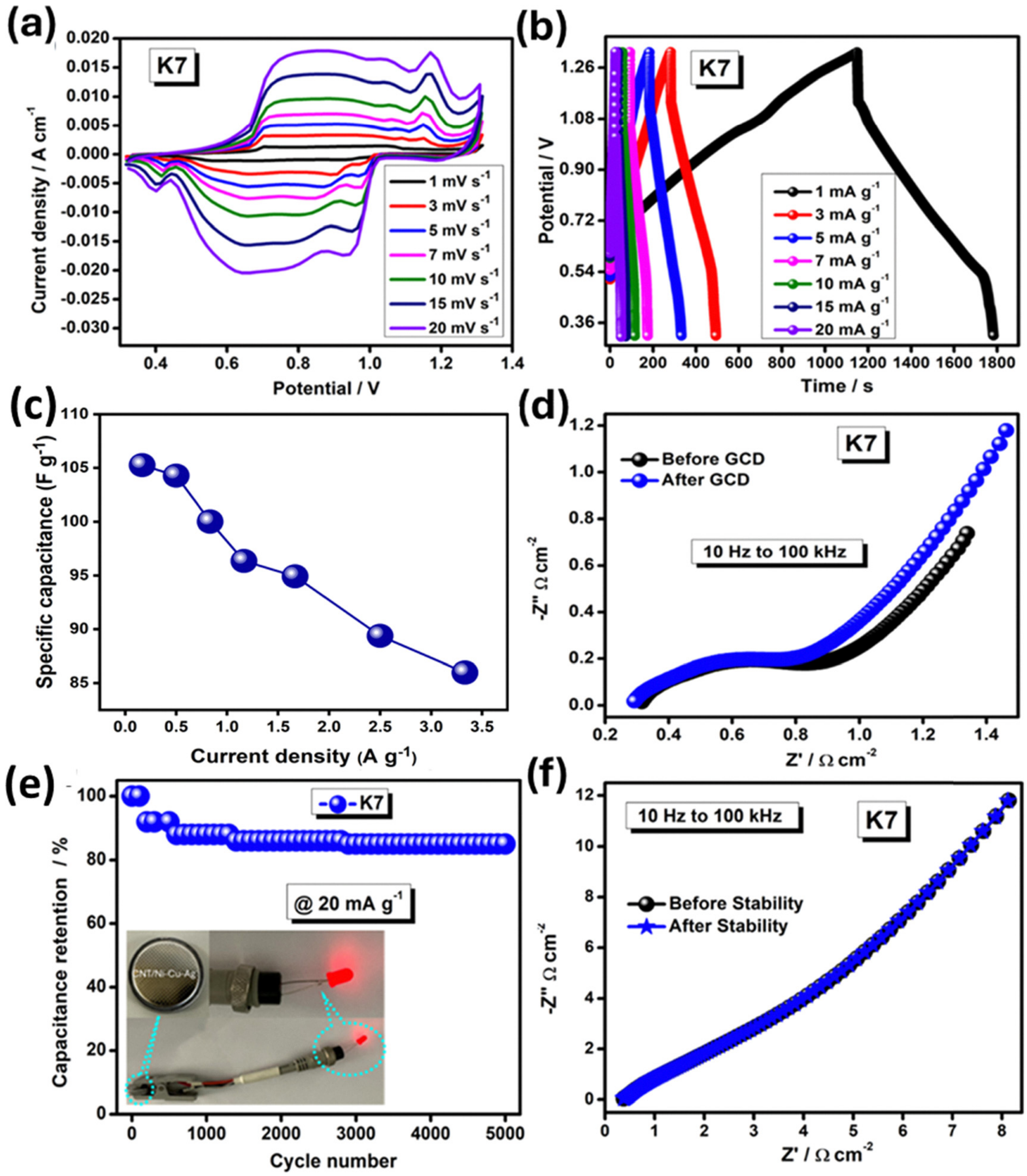

Fig. 9 Two-cell electrochemical analysis of the CNT–Ni–Cu–Ag//ASC device: (a) CV, (b) GCD, (c) specific capacitance, (d) EIS, (e) stability of CNT–Ni–Cu–Ag, and (f) EIS after the stability test.

ion diffusion, mechanical stability, and tailored electronic properties. These properties make metal-decorated CNTs highly effective for energy storage applications, such as supercapacitors.

3.9. Asymmetric supercapacitor of CNT–Ni–Cu–Ag//AC electrodes

To investigate the utilization of the CNT–Ni–Cu–Ag metal-based NCs, an asymmetric supercapacitor (ASC) device was fabricated, using activated carbon as an anode, CNT–Ni–Cu–Ag as a cathode and 6 M KOH solution as an electrolyte. In Fig. 9, the performance of the assembled CNT–Ni–Cu–Ag//AC device is shown. The fabricated ASC device was examined *via* CV, GCD and EIS analysis, under ambient conditions. In Fig. 9a, the CV curves of the ASC device tested at a fixed potential window of 1 V, under various scan speeds, are illustrated.[68] As observed, the area under the curve (peak current) gradually increased as the scan rate increased, demonstrating that the device had excellent rate performance and reversibility.

In Fig. 9b, the GCD curves are also seen at a fixed potential (1 V), under various current densities, ranging from 1 to 20 mA g^{-1}. This display showed the symmetrical charge–discharge nature of the ASC device, indicating its excellent electrochemical reversibility with high efficiency. Moreover, the ASC device displayed excellent charge storage behaviour,

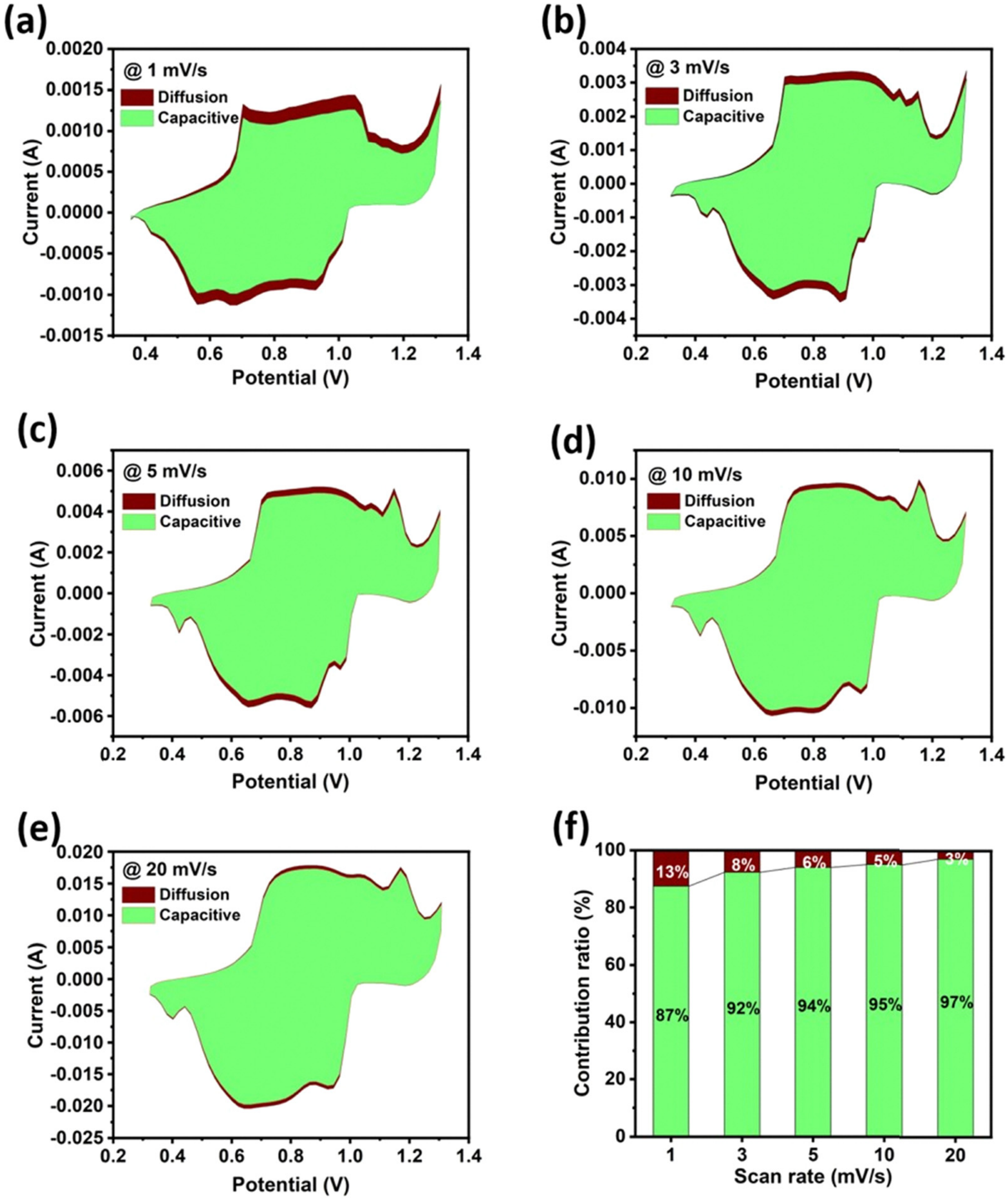

Fig. 10 Examination of charge storage characteristics using CV analysis (Dunn's approach): (a) 1 mV s^{-1}, (b) 3 mV s^{-1}, (c) 5 mV s^{-1}, (d) 10 mV s^{-1}, (e) 20 mV s^{-1}, and (f) percentage comparison of capacitive and diffusion-controlled contributions under different scan rates.

as noted by the shape of the GCD curves matching the pairs of the redox peaks of the CV profiles. The highest specific capacitance of 105 F g^{-1} was achieved through GCD analysis at a current density of 1 A g^{-1}. The specific capacitance values decreased with increasing scan rate and current density.[69] In Fig. 9c, the specific capacitance is seen to vary. Subsequently, EIS analysis was conducted to assess the interfacial resistance properties of the ASC device over a frequency at 10 Hz to 100 kHz.[70] In Fig. 9d, the Nyquist plots of the ASC device before and after GCD analysis are illustrated. The straight line inclined at low frequencies indicates Warburg impedance (W) attributed to the electrolyte diffusing into the electrode.[71]

For real-time applications, the ASC device's cyclability is essential for examining the degrading behaviour of the device. As shown in Fig. 9e, the stability of the ASC device was evaluated over 5000 cycles at a current density of 20 mA g^{-1}. At the 5000th GCD cycle, capacitance retention reached approximately 80%. In Fig. 9f, EIS measurements of the ASC device were conducted before and after stability measurements. The performance of the assembled ASC was examined through key electrochemical indicators, such as energy density and power density (Fig. S11). The device exhibited an energy density of 15 Wh kg^{-1} together with a power density of 83 W kg^{-1}, demonstrating its effectiveness in reliable energy storage. In addition, two ASC devices were connected in series and charged for 60 s, using a 1 V LED lamp.[72] Consequently, the assembled ASC device demonstrated maximum energy density and power density of 17.5 Wh kg^{-1} and 8.37 kW kg^{-1}, respectively. After

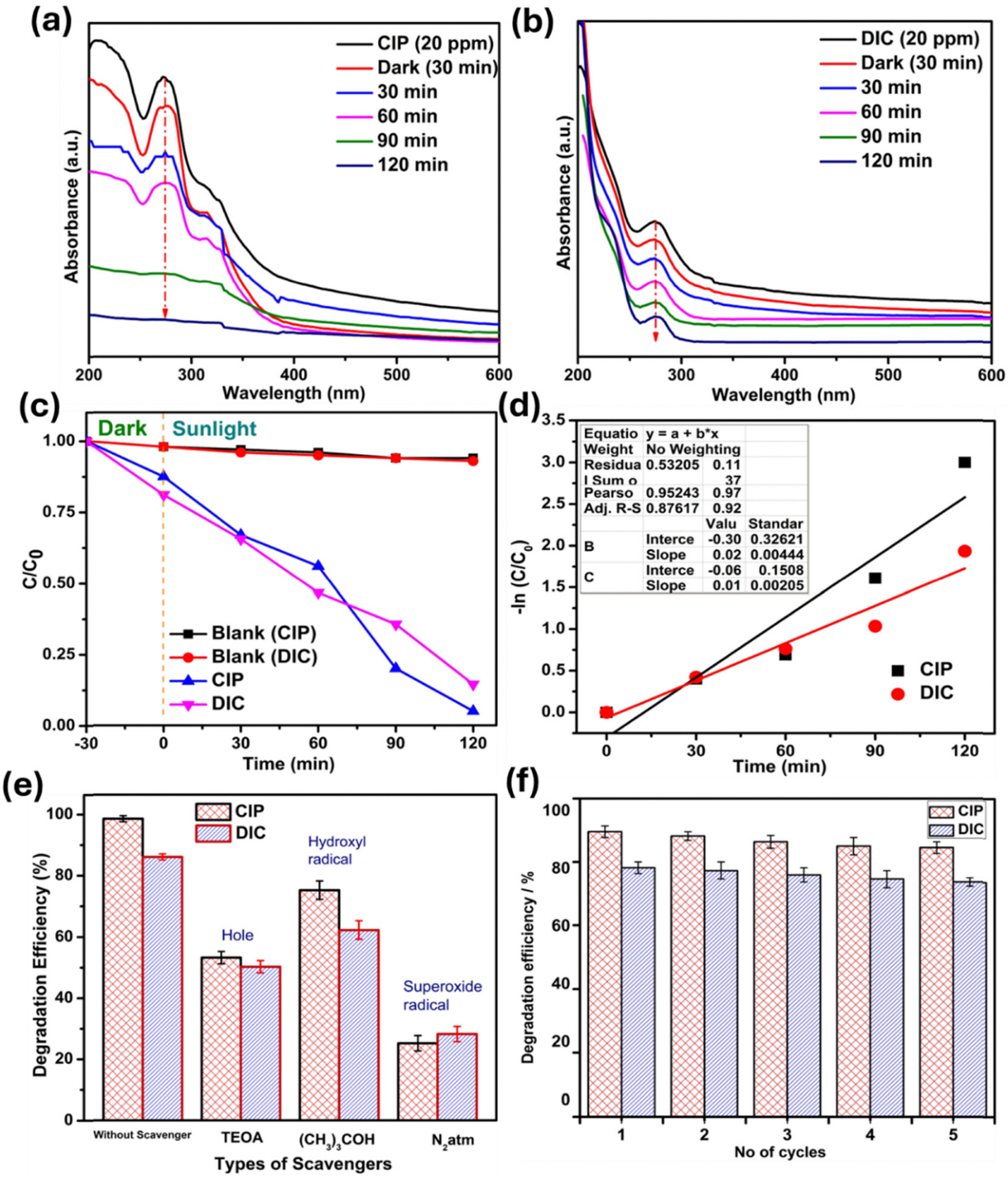

Fig. 11 Degradation graph of CNT–Ni–Cu–Ag: (a) CIP, (b) DIC for the K7 nanocomposites, (c) degradation efficiency, (d) kinetics, (e) scavenger study, and (f) reusability study graph of the CNT–Ni–Cu–Ag NPs.

careful evaluation *via* CV analysis, the charge storage kinetics of the ASC device were investigated, using Dunn's approach, as expressed in eqn (1). This approach provided information about the charge storage characteristics, which were either surface-controlled (pseudo-capacitance/capacitive) or diffusion-controlled.[72]

$$i = k_1\nu + k_2\nu \text{ or } i/\nu_{0.5} = k_1\nu_{0.5} + k_2 \quad (1)$$

In Fig. 10(a)–(e), the capacitive characteristics of the ASC device under various scan rates are shown. It is observed that as the scan rate increased, the contribution of the capacitive/surface-controlled kinetics to total capacitance increased, and diffusion-controlled contributions decreased. The capacitive contribution was found to be 87% for 1 mV s^{-1}, reaching 97% at 20 mV s^{-1} (Fig. 10f). The selective metals incorporated on CNTs exhibit high specific capacitance due to a combination of factors that enhance their electrochemical performance including increased surface area, improved electrical conductivity, pseudocapacitance contribution, synergistic effects at the metal–CNT Interface, enhanced ion diffusion, mechanical stability, and tailored electronic properties. These properties make metal-decorated CNTs highly effective for energy storage applications, such as supercapacitors.

3.10. Photocatalytic degradation of anti-inflammatory (organic pollutants)

The enhanced photocatalytic degradation performance of metal-decorated carbon nanotubes (CNTs) can be attributed to several synergistic mechanisms: improved light absorption, efficient charge separation and transfer, generation of reactive oxygen species (ROS), increased surface area and active sites, enhanced adsorption of pollutants, synergistic effects at the metal–CNT interface, and reduction of bandgap energy. These interconnected factors work together to significantly boost the photocatalytic activity of metal-decorated CNTs, making them highly effective for applications in wastewater treatment, environmental remediation, and other pollution control technologies. Here, diclofenac (DIC) and ciprofloxacin (CIP) anti-inflammatories are used for degradation. The photocatalytic degradation of DIC and CIP was analyzed under visible light, using synthesized CNT–Ni–Cu–Ag NCs, labelled as K7. In Fig. 11a, UV-visible spectra for CIP in the presence of the K7 catalyst after 2 h of visible light exposure are displayed. As CIP was treated, the pollutant concentration of CIP was seen to decrease under prolonged visible light irradiation time, indicating the decomposition of the phenyl groups in the CIP molecule. Moreover, the K7 catalyst degraded the CIP molecule, attaining an efficiency of 98.5% after 2 h. The degrading efficiency was enhanced by the combination of metal ions present on the CNT 2D-structure, which led to a faster rate of light absorption, the production of electron–hole pairs, and a delay in recombination.[73,74]

In Fig. 11b, a similar procedure was implemented. As a result, a photocatalytic organic pollutant degradation occurred when K7 NC was used against another pollutant type, the DIC solution. The K7 catalyst exhibited rapid degradation of the DIC solution and attained a degradation efficiency of 86% within 2 h of light irradiation. The significant improvement in degradation is attributed to the combination of metal NPs on the CNT surface, mitigating the recombination effect of excited charge carriers (electron–hole pairs).

In Fig. 11c, the changes in the initial and final concentrations of the organic pollutant in the presence and absence of the photocatalyst over time (t) for DIC and CIP are depicted. The K7 catalyst is seen to exhibit the highest degradation level, attributed to sub-energy levels serving as recombination traps, and a significant reduction in the band gap took place. The sub-energy level of the conduction band generated a greater number of reactive oxygen species (ROS). Further analysis of pseudo-first-order kinetics, as presented in Fig. 11d, revealed degradation rates against CIP solution of 0.010 min^{-1} and 0.0047 min^{-1}.

The effect of initial pH on the photocatalytic degradation of ciprofloxacin (CIP) and diclofenac (DIC) by the K7 composite was examined over a broad pH range (pH 4–10), as presented in Fig. S12(a) and (b). The reaction pH was adjusted using 0.1 M HCl for acidic conditions and 0.1 M NaOH for alkaline conditions. The composite exhibited its highest degradation efficiency under slightly acidic conditions, achieving 98% CIP and 86% DIC removal at pH 6. At lower pH (4–5), moderate degradation was observed, attributed to increased protonation of the pollutants and variations in catalyst surface charge. In contrast, at higher pH values (7–10), the efficiency gradually decreased, particularly for DIC, due to its predominantly anionic form, leading to electrostatic repulsion from the catalyst surface. Despite this decline, the catalyst maintained considerable activity throughout the tested pH range, confirming its robustness and practical reliability for real wastewater treatment applications, which commonly operate in slightly acidic to near-neutral conditions.

To identify the primary reactive oxygen species involved in the degradation process, studies on scavengers were conducted. The investigation into scavengers for organic pollutant degradation specifically focused on the reaction conditions with the highest degradation efficiency, which was observed for the K7 NC. Therefore, h^+, OH^-, and $^\bullet O_2^-$ were removed from the reaction solution by an accumulation of associated scavengers, such as triethanolamine (TEOA) (h^+ scavenger), *tert*-butanol ($^\bullet OH$ scavenger), and N_2-atm ($^\bullet O_2^-$ scavenger). The effectiveness of scavengers on DIC and CIP solution is shown in Fig. 11e. The scavenger experiments demonstrated that the N_2-atmosphere exhibited considerable differences in efficiency when compared to *tert*-butanol and TEOA. The superoxide radicals thus play a significant role in the breakdown of organic pollutant molecules. Reusability of photocatalysts (K7) is another crucial area of research. The results on reusability affirm the stability of the catalyst. In Fig. 11f, it is observed that even after undergoing five cycles of the photocatalytic process, there is no notable decrease in degradation efficiency. Any observed decline in degradation efficiency after five cycles is attributed to the loss of the sample during the washing process. The process elucidating the degradation of CIP and DIC organic pollutants catalysed by K7 can be expressed as follows:

(i) Generation of an electron–hole pair

$$\text{CNT–Ni–Cu–Ag} + h\nu \rightarrow \text{h}^+\ (\text{VB}) + \text{e}^-\ (\text{CB}) \tag{2}$$

(ii) Creation of hydroxyl radicals

$$\text{OH}^- + \text{h}^+ \rightarrow \text{OH}^\bullet \tag{3}$$

$$\text{H}_2\text{O} + \text{h}^+ \rightarrow \text{OH}^\bullet + \text{H}^+ \tag{4}$$

(iii) Formation of superoxide radicals

$$\text{O}_2 + \text{e}^- \rightarrow \text{O}_2^{\bullet -} \tag{5}$$

(iv) Photo degradation of CIP and DIC anti-inflammatory

$$\text{Organic pollutant} + \text{OH}^\bullet + \text{O}_2^{\bullet -} \rightarrow \text{degradation products} \tag{6}$$

The current study clearly indicates that the K7 photocatalyst exhibits superior photocatalytic degradation of DIC and CIP toxic molecules. As shown in Fig. S11, the enhanced efficiency of the K7 catalyst can be attributed to two key factors: (i) reduction in the band gap and (ii) charge trapping of the photocatalytic mechanism of K7 against DIC and CIP solution. Table S4 represents a comparison of photocatalytic activity,

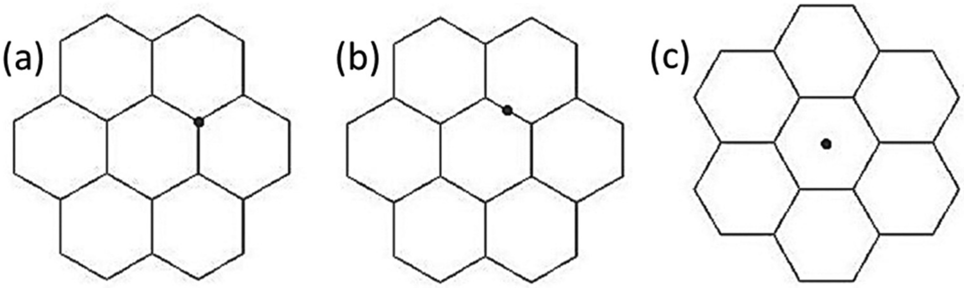

Fig. 12 Variations of the location of the metal atom relative to the surface of the carbon nanotube: (a) above the carbon atom, (b) middle of the C–C carbon bond, and (c) in the centre of the hexagon.

including recent reports.[73–84] The catalyst K7 is seen to be most effective for practical applications due to the efficient synergetic effect between CNTs and metals.

3.11. Theoretical study

To understand the physical property changes with respect to metal ions on the surface of the CNTs, theoretical studies were conducted *via* DFT using the B3LYP potential, and 6-31G basis set.[85] Processes for the formation of CNTs decorated with various transition metals: Ag, Cu, and Ni were studied. Processes of interaction of a zig-zag (6, 0) CNT with individual metal atoms (Ag, Cu and Ni) were simulated. Three possible positions for the arrangement of metal atoms relative to the CNT surface were considered: (i) above the carbon atom, (ii) in

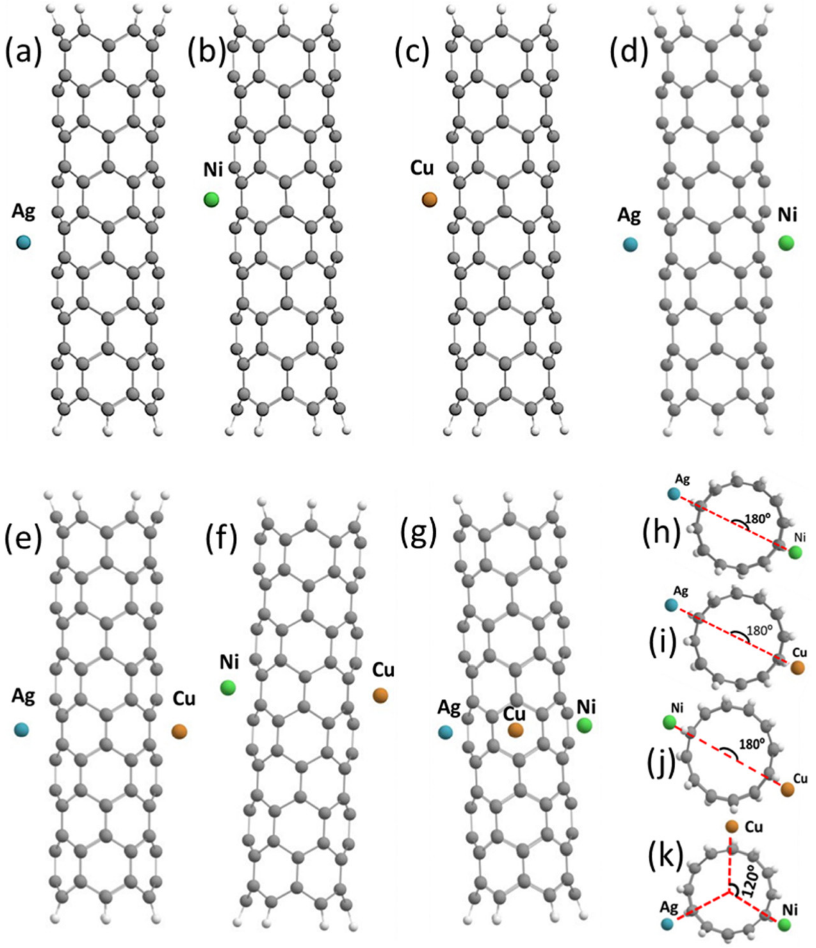

Fig. 13 The position of the metal atoms relative to the surface of the carbon nanotube: (a)–(c) the position of single atoms of Ag, Ni and Cu, (d) and (e) the position of a pair of atoms on opposite sides of a carbon nanotube: Ag–Ni, Ag–Cu, Ni–Cu, (f) and (g) the position of the three atoms Ag, Ni and Cu, (h)–(j) the position of a pair of atoms on opposite sides of a carbon nanotube: Ag–Ni, Ag–Cu, Ni–Cu, viewed from above, and (k) the position of the three atoms Ag, Ni and Cu, viewed from above.

the middle of the C–C bond, and (iii) at the centre of the carbon hexagon (Fig. 12). For modelling and theoretical studies, a molecular cluster (6, 0) nanotube was considered. The cluster contained 8 layers of carbon hexagons along the longitudinal axis of the nanotube. Unclosed valencies at the cluster boundary were closed by pseudohydrogen atoms.

The experiment was performed as follows. Selected metal atoms approached the nanotube surface step by step (with a step of 0.1 Å) along the normal to the longitudinal axis of the CNT, focusing on one of the possible surface centers – towards a carbon atom (Fig. 12a), or the center of a C–C bond (Fig. 12b), or the center of a carbon hexagon (Fig. 12c). At each step, the potential energy of the system was determined. The calculations obtained made it possible to construct the profile of the potential energy surface of the CNT–metal atom interaction and optimal distances; interaction energies were determined, as illustrated by minima on the energy curves for single, binary and ternary metallic atoms.[86]

In Fig. 13(a)–(c), the geometry of the system used in the computer experiment is observed. In the first stage, a single metal atom approached the surface of the nanotube in the manner described above. At the next stage, the interaction of the (6, 0) nanotubes with two metal atoms was studied, as shown in Fig. 13(d)–(f). Consequently, a second metal atom (Ni or Cu) gradually approached from the opposite side of the nanotube with a rigidly attached Ag atom located above the centre of the C hexagon at a distance of 2.1 Å (determined at the first stage of research).[85–87] Movement took place along the normal to the longitudinal axis of the nanotube, drawn through the centres of the two opposite C hexagons, above one of which there was an Ag atom, and above the other a Ni (or Cu) atom (Fig. 13(d) and (e)). To simulate the interaction between CNTs and another pair of Ni and Cu atoms, we considered a system consisting of a CNT with a Ni atom rigidly attached to it at a distance of 1.6 Å from the center of the hexagon, to which the Cu atom was approached step by step in the manner described above (Fig. 13(f) and (g)). The angle between the metal atoms was found to be 180° (Fig. 13(h)–(j)).

Finally, a composite consisting of (6, 0) CNTs and three atoms (Ni, Ag and Cu) was formed. The investigated results are represented geometrically. The metal atoms located above the middle of the hexagons were oriented at 120° relative to each

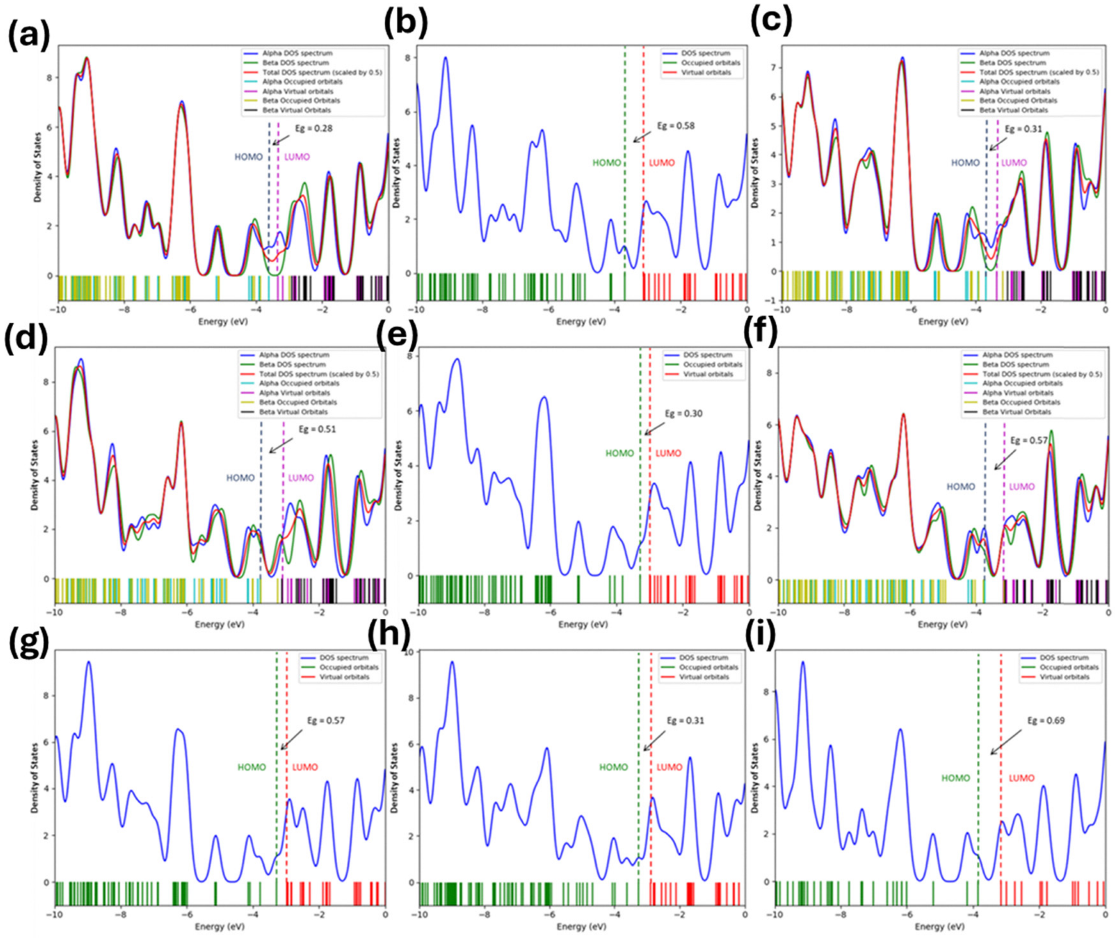

Fig. 14 The densities of states of "CNT–metal atoms" systems: (a) Ag atom, (b) Ni atom, (c) Cu atom, (d) Ag–Ni atoms, (e) Ag–Cu atoms, (f) Ni–Cu atoms, (g) CNT–Ag and Cu is added, angle between normal 120°, and (h) CNT–Ag–Cu and Ni is added, angle between normal 120°, and (i) CNT without modification.

other (Fig. 13k). The simulation was performed as follows. First, the nanotube was considered with an Ag atom rigidly fixed at a distance of 2.1 Å above the centre of the hexagon, and the copper atom was incrementally approached along the normal to the longitudinal axis of the nanotube to the centre of another hexagon. The angle between the normal drawn from the silver atom to the CNT axis and from the Cu atom to the CNT axis was 120°. Calculations made it possible to construct an energy curve for the interaction of the "CNT–Ag" system with the Cu atom, as shown in Fig. S14g. Next, the "CNT–Ag–Cu" system was fixed, and the third atom, the Ni atom, approached it step by step. The angle between the normal drawn from the silver atom to the CNT axis and from the Ni atom to the nanotube axis was also 120°. That is, all three normal vectors were drawn at the same angles of 120° relative to each other (Fig. 13k).

The calculations obtained made it possible to construct the potential energy surface profiles of these systems (Fig. S12(a)–(g)) and determine the interaction distances and energies as well as the band gap of the system (Table S5). An analysis of the results established that for all selected metal atoms, the most probable position from an energy point of view is the position of the atom above the centre of the carbon hexagon of the CNT surface (the interaction energy values are maximum in absolute value). In Fig. 14, the density of states curves for all considered "CNT–metal atom" systems are shown.

The energy gap ΔE_g was chosen as the quantity determining the electronic properties of the carbon nanotube. The value ΔE_g was calculated as the difference between the energy of the lowest unoccupied molecular orbital E_{LUMO} and the energy of the highest occupied molecular orbital E_{HOMO}:

$$\Delta E_g = E_{\mathrm{LUMO}} - E_{\mathrm{HOMO}} \tag{7}$$

An analysis of the results obtained established that the presence of metal atoms on the surface of CNTs reduces the bandgap width compared to pure CNTs (without metals). However, in the presence of a Ni atom, this decrease is not so significant. This trend continues when CNTs are simultaneously modified with Ag and/or Cu and Ni atoms (Table S5). As for the charge distribution in the systems established, it is noted that electron density is transferred from the metal atom to the nearest C atoms of the surface. Hence, the charge disturbance caused by the metal decays within the radius of the second neighbors relative to the atomic location (Table S6).

4. Conclusions

In summary, high-quality CNT-based nanocomposites (NCs) incorporating various metal nanoparticles (NPs) were synthesised *via* a simple, cost-effective chemical co-precipitation method, demonstrating remarkable potential for multifunctional applications such as the oxygen evolution reaction (OER), supercapacitors (SC), and the degradation of organic pollutants. Comprehensive structural, interfacial, and morphological analyses were conducted using advanced microscopic and spectroscopic techniques. Among the synthesised nanocomposites, the K7 NCs exhibited exceptional OER activity, delivering a current density of 50 mA cm^{-2} at an overpotential of 382 mV in 1 M KOH. Supercapacitor performance was systematically evaluated across all catalysts, with specific capacitance values recorded as follows: 838 F g^{-1} for K1, 500 F g^{-1} for K2, 912 F g^{-1} for K3, 1085 F g^{-1} for K4, 1116 F g^{-1} for K5, 1086 F g^{-1} for K6, and a peak high specific capacitance value of 1451 F g^{-1} for K7. Furthermore, under visible-light irradiation, the K7 NC exhibits excellent photocatalytic performance, efficiently degrading the pharmaceutical pollutants ciprofloxacin (CIP) and diclofenac (DIC). The nanocomposite achieves photodegradation efficiencies of 98.5% for CIP and 86% for DIC within 2 hours. The remarkable multifunctionality of the CNT–Ni–Cu–Ag nanocomposites, reflected in their superior electrochemical and photocatalytic behaviour, highlights their strong potential for practical applications in both energy storage and environmental remediation. In addition, their scalable, rapid, and cost-effective synthesis further strengthens their promise as advanced materials for next-generation energy and environmental technologies.

Conflicts of interest

There are no conflicts to declare.

Data availability

The data supporting this article have been included as part of the supplementary information (SI). The supplementary information includes UV–Vis spectra, Raman spectra, EDAX and XPS analyses, a Ragone plot, and comparative tables for photocatalytic and electrochemical supercapacitor performance. See DOI: https://doi.org/10.1039/d5ma00974j.

References

1 D.-E. Lee, A. Husain, K. Anwar, M. Danish and W.-K. Jo, *Coord. Chem. Rev.*, 2025, **545**, 217022.
2 D.-E. Lee, M. Danish, A. Husain and W.-K. Jo, *J. Alloys Compd.*, 2024, **1000**, 175048.
3 A. T. Lawal, *Carbon Trends*, 2025, **19**, 100470.
4 A. C. Dillon, *Chem. Rev.*, 2010, **110**, 6856–6872.
5 D.-E. Lee, A. Husain, A. Khan, M. Danish and W.-K. Jo, *Environ. Res.*, 2025, **264**, 120367.
6 J. Joy, J. Mathew and S. C. George, *Int. J. Hydrogen Energy*, 2018, **43**, 4804–4817.
7 U. Sohail, E. Pervaiz, M. Ali, R. Khosa, A. Shakoor and U. Abdullah, *FlatChem*, 2022, **35**, 100404.
8 R. Khosa, E. Pervaiz, U. Abdullah, M. Ali, U. Sohail and A. Shakoor, *Mol. Catal.*, 2022, **528**, 112514.
9 L. Liu, X. Zhang, X. Xie, J. Cai, J. Ding, Q. Cai, Y. Liu and S. Lu, *Int. J. Hydrogen Energy*, 2022, **47**, 26978–26986.
10 T. Ishaq, M. Yousaf, I. Ahmad Bhatti, M. Ahmad, M. Ikram, M. U. Khan and A. Qayyum, *Int. J. Hydrogen Energy*, 2020, **45**, 31574–31584.
11 I. A. Mkhalid, *Ceram. Int.*, 2022, **48**, 1542–1549.

12 X. Zhang, P. Yang and S. P. Jiang, *Carbon*, 2021, **175**, 176–186.

13 X. Zhang, P. Yang and S. P. Jiang, *Int. J. Hydrogen Energy*, 2021, **46**, 2065–2074.

14 H.-F. Wang, C. Tang and Q. Zhang, *Catal. Today*, 2018, **301**, 25–31.

15 N. Yuan, Q. Jiang, J. Li and J. Tang, *Arabian J. Chem.*, 2020, **13**, 4294–4309.

16 T. V. M. Sreekanth, G. R. Dillip, P. C. Nagajyothi, K. Yoo and J. Kim, *Appl. Catal., B*, 2021, **285**, 119793.

17 Y. Lin, S. Wu, X. Li, X. Wu, C. Yang, G. Zeng, Y. Peng, Q. Zhou and L. Lu, *Appl. Catal., B*, 2018, **227**, 557–570.

18 D.-E. Lee, A. Khan, A. Husain, K. Anwar, H.-C. Lee, S.-H. Shin, J.-Y. Lee, M. Danish and W.-K. Jo, *J. Alloys Compd.*, 2025, **1022**, 179820.

19 A. T. Hoang, S. Nižetić, C. K. Cheng, R. Luque, S. Thomas, T. L. Banh, V. V. Pham and X. P. Nguyen, *Chemosphere*, 2022, **287**, 131959.

20 A. Pajor-Świerzy and K. Szczepanowicz, *Nanotechnol., Sci. Appl.*, 2025, **18**, 197–210.

21 W. M. Daoush and S. H. Hong, *J. Exp. Nanosci.*, 2013, **8**, 742–751.

22 D. Wang, D. Li, J. Muhammad, Y. Zhou, A. Shah, X. Dong and Z. Zhang, *Phys. Status Solidi B*, 2019, 1800557.

23 I. Shakir, Z. Almutairi, S. S. Shar and A. Nafady, *Ceram. Int.*, 2022, **48**, 11278–11285.

24 T. Borkar, J. Hwang, J. Y. Hwang, T. W. Scharf, J. Tiley, S. H. Hong and R. Banerjee, *J. Mater. Res.*, 2014, **29**, 761–769.

25 G. Murugadoss, N. Kandhasamy, M. R. Kumar, A. K. Alanazi, F. A. K. Khan, B. Salhi and H. M. Yadav, *Inorg. Chem. Commun.*, 2023, **155**, 111013.

26 S. R. Mangishetti, D. Jang, J. Choi, G. Rajeshkhanna, S. Pittala, S. K. Kang, J. Ji, M. Kim, S. G. Jung, J. Ha, J. Kim, J. Maeng, G. H. Park, J. Bae and W. B. Kim, *Chem. Eng. J.*, 2023, **472**, 144863.

27 K. L. Chitturi, S. Garimella, A. K. Marapaka, K. R. Kudle and R. Merugu, *J. Bionanosci.*, 2018, **12**, 284–289.

28 H. Fayazfar, A. Afshar and A. Dolati, DOI: 10.4236/msa.2013.411083.

29 M. Danish, Z. Rasool, H. Iqbal, R. Fatima, S. Kumar and M. Muneer, *Mater. Adv.*, 2023, **4**, 3506–3520.

30 S. Tang, L. Li, X. Cao and Q. Yang, *Heliyon*, 2023, **9**, e13523.

31 S. D. M. Brown, M. S. Dresselhaus, A. Jorio and G. Dresselhaus, *Phys. Rev. B: Condens. Matter Mater. Phys.*, 2001, **64**, 3–6.

32 Z. Meić, M. Žinić, S. Miljanić, L. Frkanec and T. Biljan, *J. Raman Spectrosc.*, 2007, **38**, 1538–1553.

33 K. L. Chitturi, S. Garimella, A. K. Marapaka, K. R. Kudle and R. Merugu, *J. Bionanosci.*, 2018, **12**, 284–289.

34 Z. Yang, L. Wang, Z. Shi, M. Wang, Y. Cui, B. Wei, S. Xu, Y. Zhu and W. Fei, *Carbon*, 2018, **127**, 329–339.

35 X. Zhang, Y. Zhang, B. Tian, Y. Jia, M. Fu, Y. Liu, K. Song, A. A. Volinsky, X. Yang and H. Sun, *J. Mater. Sci. Technol.*, 2020, **37**, 185–199.

36 Q. Zhang, C. Cai, J. Qin and B. Wei, *Nano Energy*, 2014, **4**, 14–22.

37 A. Pulido, P. Concepción, M. Boronat, C. Botas, P. Alvarez, R. Menendez and A. Corma, *J. Mater. Chem.*, 2012, **22**, 51–56.

38 S. Chen, S. Fu, D. Liang, X. Chen, X. Mi, P. Liu, Y. Zhang and D. Hui, *Nanotechnol. Rev.*, 2020, **9**, 146–154.

39 F. Daneshvar, T. Zhang, A. Aziz, H.-J. Sue and M. E. Welland, *Carbon*, 2020, **157**, 583–593.

40 M. Lenglet, F. Hochu, J. Dürr and M. H. Tuilier, *Solid State Commun.*, 1997, **104**, 793–798.

41 M. Jung, P. Sivakumar and H. S. Park, *J. Phys.: Energy*, 2023, **5**, 25005.

42 K. S. Kim, *Chem. Phys. Lett.*, 1974, **26**, 234–239.

43 Y. Li, H. Zhang, B. Wu and Z. Guo, *Appl. Surf. Sci.*, 2017, **425**, 194–200.

44 T. C. Kaspar, T. C. Droubay, S. A. Chambers and P. S. Bagus, *J. Phys. Chem. C*, 2010, **114**, 21562–21571.

45 N.-Y. Kim, Y.-C. Leem, S.-H. Hong, J.-H. Park and S.-Y. Yim, *ACS Appl. Mater. Interfaces*, 2019, **11**, 6363–6373.

46 Y. Zhang, B. Lin, Y. Sun, X. Zhang, H. Yang and J. Wang, *RSC Adv.*, 2015, **5**, 58100–58106.

47 X. Guan, L. Cao, Q. Huang, D. Kong, P. Zhang, H. Lin, W. Li, Z. Lin and H. Yuan, *Polymers*, 2015, **44**(12), 4091–4130.

48 R. Ranjithkumar, S. E. Arasi, S. Sudhahar, N. Nallamuthu, P. Devendran, P. Lakshmanan and M. K. Kumar, *Phys. B*, 2019, **568**, 51–59.

49 Y. Zhang, X. Sun, L. Pan, H. Li, Z. Sun, C. Sun and B. K. Tay, *J. Alloys Compd.*, 2009, **480**, L17–L19.

50 A. Subagio, A. Darari, I. S. Hakim, P. Priyono, P. Pardoyo and A. Subhan, *Mater. Sci. Forum*, 2018, **929 MSF**, 121–127.

51 K. Tai, X. He, X. Yuan, K. Meng, Y. Gao and F. Yuan, *Colloids Surf., A*, 2017, **518**, 218–231.

52 Y. J. Kang, B. Kim, H. Chung and W. Kim, *Synth. Met.*, 2010, **160**, 2510–2514.

53 J. R. Xavier, S. P. Vinodhini and S. S. Chandraraj, *J. Cluster Sci.*, 2023, **34**, 1805–1817.

54 Z.-D. Huang, B. Zhang, R. Liang, Q.-B. Zheng, S. W. Oh, X.-Y. Lin, N. Yousefi and J.-K. Kim, *Carbon*, 2012, **50**, 4239–4251.

55 X. Guan, L. Cao, Q. Huang, D. Kong, P. Zhang, H. Lin, W. Li, Z. Lin and H. Yuan, *Polymers*, 2019, **11**(6), 973.

56 A. Subagio, A. Darari, I. S. Hakim, P. Priyono, P. Pardoyo and A. Subhan, *Mater. Sci. Forum*, 2018, **929 MSF**, 121–127.

57 Q. Liu, J. Yang, X. Luo, Y. Miao, Y. Zhang, W. Xu, L. Yang, Y. Liang, W. Weng and M. Zhu, *Ceram. Int.*, 2020, **46**, 11874–11881.

58 G. K. Maron, J. H. Alano, B. da Silveira Noremberg, L. da Silva Rodrigues, V. Stolojan, S. R. P. Silva and N. L. Villarreal Carreño, *J. Alloys Compd.*, 2020, **836**, 155408.

59 G. Xu, C. Zheng, Q. Zhang, J. Huang, M. Zhao, J. Nie, X. Wang and F. Wei, *Nano Res.*, 2011, **4**, 870–881.

60 Y.-H. Lai, S. Gupta, C.-H. Hsiao, C.-Y. Lee and N.-H. Tai, *Electrochim. Acta*, 2020, **354**, 136744.

61 H. Yi, H. Wang, Y. Jing, T. Peng, Y. Wang, J. Guo, Q. He, Z. Guo and X. Wang, *J. Mater. Chem. A*, 2015, **3**, 19545–19555.

62 S. Kong, K. Cheng, T. Ouyang, K. Ye, G. Wang and D. Cao, *J. Electroanal. Chem.*, 2017, **786**, 35–42.

63 W.-S. Li, Y.-C. Shih and H.-C. Cheng, *Chem. Phys. Lett.*, 2020, **750**, 137499.

64 A. Chinnappan, H. Bandal, H. Kim and S. Ramakrishna, *Chem. Eng. J.*, 2017, **316**, 928–935.

65 J. Zhang, J. Zang, Y. Wang, G. Xin and Y. Zhang, *RSC Adv.*, 2014, **4**, 64162–64168.

66 D. Ganguly, D. Pahari, N. S. Das, P. Howli, B. Das, D. Banerjee and K. K. Chattopadhyay, *J. Electroanal. Chem.*, 2016, **778**, 12–22.

67 X. Tan, S. Liu, Q. Guo, J. Zhang, S. Liang, M. He and J. Luo, *Int. J. Energy Res.*, 2020, **44**, 4556–4567.

68 D. J. Patil, D. B. Malavekar, J. H. Kim and C. D. Lokhande, *J. Energy Storage*, 2023, **72**, 108729.

69 A. H. Anwer, M. Z. Ansari, F. Mashkoor, S. Zhu, M. Shoeb and C. Jeong, *J. Alloys Compd.*, 2023, **955**, 170038.

70 M. Pal and K. M. Subhedar, *Energy Storage Mater.*, 2023, **57**, 136–170.

71 H. Xu, J. Zhu, M. Xu, Z. Lei, Q. Hu and X. Jin, *J. Colloid Interface Sci.*, 2023, **645**, 974–984.

72 J. Dangbegnon, N. Garino, M. Angelozzi, M. Laurenti, F. Seller, M. Serrapede, P. Zaccagnini, P. Moras, M. Cocuzza, T. Ouisse, H. Pazniak, J. Gonzalez-Julian, P. M. Sheverdyaeva, A. Di Vito, A. Pedico, C. F. Pirri and A. Lamberti, *J. Energy Storage*, 2023, **63**, 106975.

73 G. Murugadoss, D. D. Kumar, M. R. Kumar, N. Venkatesh and P. Sakthivel, *Sci. Rep.*, 2021, **11**, 1–13.

74 A. Padmanaban, G. Murugadoss, N. Venkatesh, S. Hazra, M. Rajesh Kumar, R. Tamilselvi and P. Sakthivel, *J. Environ. Chem. Eng.*, 2021, **9**, 105976.

75 M. Salari, G. R. Rakhshandehroo, M. R. Nikoo, M. M. Zerafat and M. G. Mooselu, *Environ. Technol. Innovation*, 2021, **23**, 101625.

76 H. Wang, J. Li, P. Huo, Y. Yan and Q. Guan, *Appl. Surf. Sci.*, 2016, **366**, 1–8.

77 M. Shkir, T. H. AlAbdulaal, M. Ubaidullah and V. Reddy Minnam Reddy, *Chemosphere*, 2023, **338**, 139432.

78 M. Salari, *Adv. Appl. NanoBio-Technol.*, 2022, **3**, 82–86.

79 A. Avcı, İ. İnci and N. Baylan, *J. Mol. Struct.*, 2020, **1206**, 127711.

80 M. Yousefi, M. Farzadkia, A. H. Mahvi, M. Kermani, M. Gholami and A. Esrafili, *Chemosphere*, 2024, **349**, 140972.

81 N. Aghababaei, M. Abdouss, H. Hosseini-Monfared and F. Ghanbari, *J. Water Process Eng.*, 2023, **53**, 103702.

82 M. Sadeghi, M. H. Mehdinejad, N. Mengelizadeh, Y. Mahdavi, H. Pourzamani, Y. Hajizadeh and M. R. Zare, *J. Water Process Eng.*, 2019, **31**, 100852.

83 Y. Huaccallo, S. Álvarez-Torrellas, M. P. Marín, M. V. Gil, M. Larriba, V. I. Águeda, G. Ovejero and J. García, *Environ. Sci. Pollut. Res.*, 2019, **26**, 22372–22388.

84 M. Masjoudi, M. Golgoli, Z. Ghobadi Nejad, S. Sadeghzadeh and S. M. Borghei, *Chemosphere*, 2021, **263**, 128043.

85 M. Ghorbani-Asl, P. D. Bristowe and K. Koziol, *Phys. Chem. Chem. Phys.*, 2015, **17**, 18273–18277.

86 J. Lee, T. Sadi, V. Georgiev, A. Todri-Sanial and A. Asenov, *Hal-Lirmm.Ccsd.Cnrs.Fr*, 2017, pp. 1–3.

87 J. Kazerovskis, S. Piskunov, Y. F. Zhukovskii, P. N. D'Yachkov and S. Bellucci, *Chem. Phys. Lett.*, 2013, **577**, 92–95.